

Anisotropic anomalous diffusion in microgravity dusty plasma. Part One: Nonequilibrium Statistical Analysis

Bradley R. Andrew¹, Luca Guazzotto¹, Uwe Konopka¹, Lorin Matthews², Hyde Truell²,
and E. G. Kostadinova¹

¹*Physics Department, Auburn University, Auburn, Alabama, USA*

²*Center for Astrophysics Space Physics and Engineering Research (CASPER), Baylor University, Waco,
Texas, USA*

Abstract

Anisotropic anomalous dust diffusion in microgravity dusty plasma is investigated using experimental data from the Plasmakristall-4 (PK-4) facility on board the International Space Station. The PK-4 experiment uses video cameras to track individual dust particles, which allows the collection of large amounts of statistical information on the dust particle positions and velocities. These statistics are used to quantify anomalous dust diffusion caused by anisotropies in the plasma-mediated dust-dust interactions in PK-4. Anisotropies are caused by an externally applied polarity-switched electric field, which modifies the ion wakefields surrounding the dust grains. Video data for nine sets of pressure-current conditions are used to recover Mean Squared Displacement (MSD) plots after subtracting particle drift. Position and velocity histograms are fitted to Tsallis nonextensive probability distribution functions (PDFs). Both MSDs and PDFs indicate a crossover from suprathermal to Lévy diffusion in the axial direction at higher pressure conditions. In addition, increasing the pressure enhances dust thermal equilibrium, while increasing the current drives the system away from equilibrium.

1 Introduction

Complex (or dusty) plasmas are a collection of electrons, ions, neutral particles, and dust grains (typically micro- to nano-meter in size). Dusty plasma is ubiquitous in astrophysical and space environments, as well as in laboratory settings, both on Earth and in microgravity. Dusty plasma is a unique analogue system for the study of complex phenomena such as phase transitions, anomalous diffusion, and metastability. The particles in these systems are visible at the kinetic level, thus allowing for a reconstruction of the entire phase space. In addition, particle tracking or velocimetry techniques can be used to obtain statistically significant amount of data. Finally, dusty plasma experiments are reasonably simple to build (table-top) and highly controlled, which makes them ideal for deployment in space. Due to the complex interactions among the different charged species, dusty plasmas are observed to exhibit various waves, instabilities, and nonlinear structures [1, 2]. Dusty plasmas are also ideal for studying solid-liquid phase transitions [3, 4, 5, 6], electroheology [7, 8], strong interparticle coupling and long-range interactions [9, 10, 11], kinetic theories and diffusion properties [12, 13, 14, 15, 16], and critical phenomena such as melting and crystallization [6, 16, 17], and turbulence [18, 19, 20]. As they exhibit many-body effects, dusty plasmas are useful analogue systems for the study of complex systems such as condensed matter [21, 18] and smart materials [22, 7, 23]. Many other physical aspects and applications of dusty plasma have been summarized in several recent overview papers [24, 25, 26]. With all the characteristics described above, dusty plasmas are ideal for testing new analytical models, especially those focused on non-equilibrium or non-extensive statistics, anomalous diffusion, and stochasticity [18, 27, 28, 29, 30, 14, 15].

Here we investigate dusty plasma experiments conducted in the Plasmakristall-4 (PK-4) facility on board the International Space Station, where the microgravity environment allows to neglect gravity and confinement forces, thus, focusing on plasma-mediated dust-dust interactions. Recent studies using the PK-4 facility [31] have investigated various dynamical phenomena, including dust ionization waves [32], ion density waves [33], dust acoustic waves [34], unsteady shear flows and flow patterns fluctuations [35], and lunar atmosphere dust [36]. Additionally, analysis of PK-4 data has inspired a breadth of numerical studies, including particle-in-cell simulation of PK-4 predicting the formation of ionization waves [37] and molecular dynamics simulations of dust and ions investigating how such ionization waves can cause anisotropies in the ion wakefields around the dust grains [38, 39].

The PK-4 experiment uses video cameras to track individual dust particles, which allows for obtaining large amounts of statistical information on the dust particles positions and velocities. Previous studies of dusty plasma with the PK-4 experiment have shown velocity distribution functions (VDFs) that were non-Maxwellian, had high-energy tails, and displayed anomalous diffusion. Anomalous diffusion is a microscopic process which leads to a mean squared displacement (MSD) that grows non-linearly with time $MSD \propto \tau^\alpha$, where τ is time delay. If the MSD growth is faster than linear with time, $\alpha > 1$, the particles are superdiffusive, while growth rate slower than linear, $\alpha < 1$, indicates subdiffusion. Anomalous diffusion and corresponding non-linear MSDs have been observed in biological molecular transport [40], Lévy flight movement patterns of living organisms [41], condensed matter physics [42], and dusty plasmas [43, 14, 30]. A review of classical and anomalous diffusion across many fields can be found in [44]. A major goal of the present paper is to promote the use of Tsallis nonequilibrium statistics in dusty plasma analysis, since it provides greater clarity to the classification and study of nonequilibrium systems, non-Maxwellian distributions, and the resulting anomalous diffusion.

Here we analyze anomalous diffusion and thermodynamic nonequilibrium properties by constructing MSD plots and histograms of dust displacements and velocities. Nonextensive (Tsallis) statistics [45, 46, 47, 48, 49, 50, 51] is used to quantify how dust PDFs deviate from a Gaussian/Maxwellian distribution and to identify the sub-regime of anomalous diffusion that best describe each dataset. Nonextensive statistics (also called nonequilibrium statistics) is a formulation of statistical mechanics where entropies are nonadditive (nonextensive). Nonextensive statistics has been used in plasma physics to better understand solar wind turbulence and dynamics [52, 53], plasma waves [54, 55, 56], collisions [57], dusty plasmas [58, 59], including analysis of previous PK-4 experiments using combined DC-RF discharge [30, 15, 14]. We build on these previous studies by analyzing PK-4 data from pure DC discharge experiments where the dust clouds was shown to exhibit strongly non-isotropic filamentary structure.

We investigate nine pressure-current datasets from PK-4 experiments conducted in pure DC neon discharge. The negatively-charged dust particles are kept stationary in the field of view of the particle observation cameras by switching the polarity of an externally-applied electric field. As the frequency of the polarity switching (500Hz) is higher than the typical dust response frequency, the dust experiences net zero force due to the electric field. This, however, results in an anisotropy in the ion wakefields surrounding the dust, which in turn causes anisotropic dust diffusion. Particle tracking techniques [60] were used to obtain the dust positions and velocities from video data. The dust MSD, the displacement histograms, and the velocity histograms were reconstructed using the open-sourced `@msdanalyzer` code [40]. Table 1 below provides a summary of the plasma conditions and dust density for each analyzed case.

Data Set	1	2	3	4	5	6	7	8	9
P [Pa]	28.5	28.5	28.5	46.1	46.1	46.1	70.5	70.5	70.5
I [mA]	0.35	0.7	1	0.35	0.7	1	0.35	0.7	1
n [mm ⁻³]	81.8	88	85.3	123.6	93.4	93.3	55.1	93.3	69.3

Table 1: Pressure, current, and dust density for each examined data set from PK-4 experiments.

Fits to the MSDs plots reveal a non-linear relation with time delay τ^α , which is indicative of anomalous diffusion. Fits to both the position and velocity histograms for the direction along the external electric field are best described by a q-Gaussian distribution function instead of a Gaussian or a Maxwellian one. We use scaling relations proposed in literature to compare the nonextensive q_p exponent found from fits to displacement histograms against the MSD exponent α to validate the sub-regime of observed anomalous diffusion. The dust displacements and velocities in the direction perpendicular to the external electric field are best described by a Bi-q-Gaussian distribution. This suggests that the system has two distinct thermodynamic populations. As the neutral gas pressure in dusty plasma mediates the dust-neutral collisions, increasing pressure in these experiments acts as decreasing temperature, which is why the observed thermodynamics is sensitive to pressure changes. This was also seen by [61], which conducted a structural analysis of the same set of experiments using pair correlation function techniques. The remainder of this paper is dedicated to the qualitative and quantitative description of the observed anomalous diffusion, anisotropies, and equilibrium properties of dusty plasma in PK-4.

The remainder of this paper is organized as follows. An overview of the experimental setup used for the PK-4 experiment is provided in (section 2). A summary of nonextensive statistics and its application to anomalous diffusion is given in (section 3). The statistical and fitting tools used for the analysis are described in (section 4). A summary of results is presented in (section 5) followed by a discussion in (section 6). Conclusions and future work are outlined in (section 7).

2 Experimental Setup

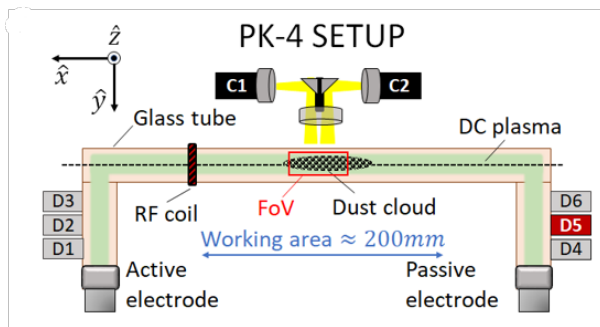


Figure 1: PK-4 Experimental Setup. Dust moves into camera FoV.

Here we briefly discuss the PK-4 experimental apparatus [31], and the specifics of the Campaign 7 (C7) data that we use for the analysis. The core of PK-4 comprises an integrated baseplate housing

the diverse components, including a glass plasma chamber with electrodes and microparticle dispensers (injecting Melamine-Formaldehyde spheres), vacuum and gas supply systems, plasma generation and diagnostic tools, microparticle manipulation devices, a microparticle observation system with cameras, and an illumination laser, see Figure 1. The main vacuum vessel is a cylindrical glass chamber, where plasma can be created using a dc discharge power supply. Polarity switching of the dc current at different frequencies and variable duty cycles can be used to transport the dust particles (using an asymmetric duty cycle) and capture them in the cameras field of view (using a symmetric duty cycle). Several microparticle manipulation options and on-board plasma diagnostics, such as a plasma glow observation system and a mini spectrometer, are also available. Here we label the axial direction in PK-4 (x direction in 1) as \parallel since it is parallel to the direction of the dc electric field. The radial, or cross-field, direction in the cameras field of view (z direction in 1) will be labeled \perp .

The DC discharge plasma is generated by two electrodes within a π -shaped glass chamber. A custom-made bipolar high-voltage (HV) power supply serves as a current source, providing a stabilized output current up to 3.1 mA at a maximal overall voltage of 2.7 kV. The current is regulated on the active side, with return current measurement on the passive side. Steady-state deviations from the set current value remain below 5%. When symmetric duty cycle is used with a fast polarity switching of the current (here 500 Hz), the dust microparticles are unresponsive as dust response frequency is close to 10 Hz. This results in overall stationary negatively charged microparticles suspended within a slowly 'sloshing' stream of ions that forms anisotropic ion wakefields surrounding the dust grains. The Particle Observation (PO) system facilitates microparticle imaging, employing a 532 nm diode laser and two PO cameras with CCD chips of 1600×1200 pixels. The cameras are movable and can cover the entire volume of the working area.

The PK-4 Campaign 7 experiments discussed here were conducted on July 26, 2019. Our analysis uses the video data from nine sets of pressure-current conditions (see Table 1). The current polarity switching was 500 Hz with a duty cycle of 50%, and microparticle size of $3.38\mu\text{m}$ diameter. In each case, the dust cloud was allowed to settle for 50 s, after which a scan of the laser sheet was performed through the dust cloud (along the y-axis in 1). These y-scans allow for obtaining information on the 3D structure of the cloud. The statistical analysis presented here uses particle tracking data obtained for a period in which the dust cloud has settled and that the cameras and laser sheet are focused on the mid-plane of the cloud. We use the dust particle positions and velocities to study the probability distribution functions, anomalous diffusion, temperature, and nonequilibrium properties.

3 Statistical Approach to Anomalous Diffusion

3.1 Diffusion

In the absence of long-range interactions or correlations, the particle diffusion can be described by Brownian motion and the model differential equation is the well-known diffusion equation

$$\frac{\partial p(x, t)}{\partial t} = \Delta(Dp(x, t)), \quad (1)$$

where $\Delta = \frac{\partial^2}{\partial x^2}$ is the Laplacian operator, D is the diffusion constant, and $p(x, t)$ is the distribution function. Equation 1 is also the linear Fokker-Planck equation with no drift. The one-dimensional solution to the diffusion equation has a Gaussian distribution functional form given by

$$p(x, t) = \frac{1}{\sqrt{2\pi Dt}} e^{-\frac{(x-x_0)^2}{2Dt}}. \quad (2)$$

The mean squared displacement (MSD) is the second moment of this equation: $\langle (x - x_0)^2 \rangle \equiv \int (x - x_0)^2 p(x, t) dx = Dt$. As can be seen, the classical diffusion equation yields MSD that grows linearly with time. Assuming discrete particle positions, the MSD expression for N particles can be generalized in two or three dimensions to

$$\langle |r(t) - r_0|^2 \rangle = \frac{1}{N} \sum_{i=1}^N |r^{(i)}(t) - r^{(i)}(t=0)|^2 = 2dDt^\alpha \quad \alpha \geq 0, \quad (3)$$

where d is the dimension and α is an exponent that quantifies deviations from a linear dependence in time (i.e., the presence of anomalous diffusion). When $\alpha = 1$ (linear MSD), the diffusion is classical, while $\alpha \neq 1$ implies anomalous diffusion. While anomalous diffusion is ubiquitous in nature [40, 41, 42, 43, 14, 30, 44], its mathematical description is challenging. One way to study anomalous diffusion is with a nonlinear diffusion equation, the nonlinear Fokker-Planck differential equation, which has solutions including Porous Medium equations (see page 249 of [62]) and Tsallis q -Gaussian distributions [63] (also known as Kappa distribution or Student's t distribution). Anomalous diffusion may also be studied by use of fractional spatial derivatives [27, 29, 64, 18] which may have solutions such as Lévy distributions. We note that it is not well understood if universal scaling relations exist that link the different proposed analytical formulations for anomalous diffusion. While there are some direct relations between the nonlinear Fokker-Planck equations and the q -Gaussian solutions, their relation to fractional differential equations is not straightforward even though they can both describe similar regimes of anomalous diffusion.

3.2 The Nonlinear Diffusion Equation and Tsallis' Statistics

The nonlinear Fokker-Planck equation with no drift

$$\frac{\partial p(x, t)}{\partial t} = D \frac{\partial^2 [p(x, t)]^\nu}{\partial x^2} \quad (4)$$

has the solution

$$p(x, t) = \frac{1}{\sqrt{\pi A_q}} \left[1 + (q-1) \frac{(x-x_0)^2}{A_q (D_q t)^{\frac{1}{3-q}}} \right]^{\frac{-1}{q-1}}. \quad (5)$$

Here ν is related to the nonextensive parameter q by $\nu \equiv 2 - q$ [63]. A_q is a normalization factor given by

$$A_q = \begin{cases} \sqrt{(q-1)} \frac{\Gamma(\frac{1}{q-1})}{\Gamma(\frac{3-q}{2q-2})} & \text{if } 1 < q < 3 \\ 2 & \text{if } q = 1 \\ \sqrt{(1-q)} \frac{\Gamma(\frac{5-3q}{2-2q})}{\Gamma(\frac{2-q}{1-q})} & \text{if } q < 1. \end{cases} \quad (6)$$

The parameter q can also be related to the distribution kurtosis κ , through the following relationship: $k = \frac{15-9q}{7-5q}$, for $q < 7/5$ [65] where $k = \text{Kurtosis} = \frac{\langle x^4 \rangle}{\langle x^2 \rangle^2}$. This can be used to quantify the deviations from a Gaussian distribution and the related anomalous diffusion (e.g., as discussed in [66]). The primary interest of the present study is the range $1 < q < 3$ where the distributions exhibit leptokurtic or 'fat-tail' behavior. This regime is also where anomalous diffusion is superdiffusive ($\alpha > 1$), though we will also discuss subdiffusive cases where $q < 1$ or $\alpha < 1$ (see Figure 2 for example distributions representing each regime). Anomalous diffusion is described by taking the second moment of Eq. 5, which yields a non-linear relation between the MSD and time

$$\langle (x - x_0)^2 \rangle \propto D_q t^{\frac{2}{3-q}}; \quad q < \frac{5}{3}, \quad (7)$$

where D_q is a new diffusion coefficient. Nonextensive statistics were proposed by Tsallis [67] and are described fully in the textbook on the subject [63]. The probability distribution function in this formulation is called a q -Gaussian, where the parameter q quantifies the nonextensivity of the system. The nonextensivity feature of the formulation makes it independent of initial conditions and suitable for modeling many-body complex systems with long-range interactions, such as plasma. Systems with this nonextensive behavior no longer have additive entropies, $S_q(A+B) \neq S_q(A) + S_q(B)$, and the different microstates are not in equilibrium. Therefore, quantifying the nonextensivity is needed to make rigorous statistical claims and understand equilibrium properties of systems with long-range interactions and

correlations. Thus, q can be understood as a parameter quantifying the strength of correlations or non-local interactions causing the system to move away from equilibrium. The nonextensive parameter q can be found by extremizing the Tsallis entropy S_q with Lagrange constraints, such as normalization and moment of the distribution. Essentially, it can be thought of as the nonlinear form of the Maxwellian distribution, with normalization A_q , kinetic energies E_i , potential U , and inverse temperature β_q . This results in the following probability distribution function, known as the q -Gaussian

$$p_i = \frac{\beta_q}{A_q} e_q^{(-\beta_q(E_i - U_q))} = \frac{\beta_q}{A_q} [1 - (1 - q)\beta_q(E_i - U_q)]^{\frac{1}{(1-q)}} \quad (8)$$

Note that in the limit where $q \rightarrow 1$, the Maxwellian distribution is recovered. This is accomplished by letting the potential energy $U_q = 0$, $\beta_q = 1/(v_{qth}^2)$, where v_{qth} is the q -Gaussian thermal velocity, and $E = \frac{1}{2}mv^2$, recalling the fact that $e^x = \lim_{n \rightarrow \infty} (1 + \frac{x}{n})^n$ and letting $n = \frac{1}{1-q}$

$$\lim_{q \rightarrow 1} \frac{1}{v_{qth} A_q} [1 - (1 - q) \frac{mv^2}{2v_{qth}^2}]^{\frac{1}{(1-q)}} \rightarrow \sqrt{\frac{m}{2\pi v_{th}^2}} * e^{-\frac{mv^2}{2m v_{th}^2}}. \quad (9)$$

The relationship between the Maxwellian temperature T_M and the q -Gaussian temperature T_q was discussed in [56] and is given by

$$T_q \left(\frac{5q - 3}{2} \right) = T_M. \quad (10)$$

Eq. 10 relates the q -Gaussian variance fits (i.e. σ_q^2 , D_q , v_{qth}^2 , or T_q) to the corresponding Gaussian or Maxwellian value. This step is necessary as the kurtosis of a distribution affects the variance, which should be taken into account to find a more appropriate variance value.

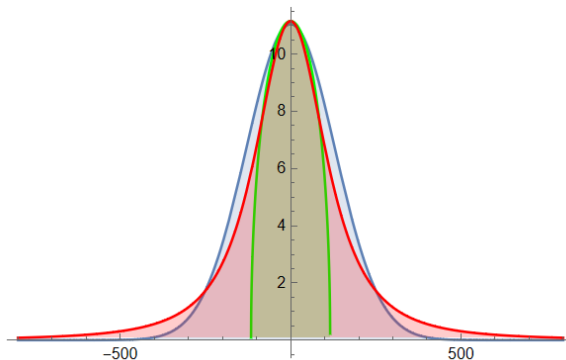


Figure 2: Analytical plot of the q -Gaussian distribution for three cases. $q = -1$ (Green), $q = 1$ (Blue), and $q = 5/3$ (Red).

Figure 2 shows different q -Gaussian distributions scaled to the same height to exemplify how the distribution shape deviates from a Gaussian ($q = 1$) for different values of the nonextensive parameter q . Equation 5 and Eq. 8 have the same functional form, but have different variables, coefficients, and exponents as the former is in position space, while the latter is in velocity space. In this paper, we distinguish between the two by using q_p and q_v , respectively. The variances of these distributions are finite for $q < 5/3$ but diverge for $5/3 \leq q < 3$. This means that, as $N \rightarrow \infty$, the distribution approaches a Gaussian for $q < 5/3$, while, for $5/3 \leq q < 3$, it approaches a Lévy distribution. For the position displacement distributions, $q_p > 5/3$ the diffusion is a Lévy process which yields large 'jumps' or Lévy flights. Since we utilize the notation q_v , we call a process 'energetic' or 'suprathedral' if $q_v > \frac{4+d}{2+d}$, where d is the dimensionality. Thus, for $d = 1$, $q > \frac{5}{3}$ there are 'large jumps' in velocity space, as expected for a Lévy process. For $q < \frac{5}{3}$ (implying the mathematical variance is finite), there are no Lévy processes or Lévy flights. In part two of this paper, "Spectral Analysis" we will go into more detail on this topic and the use of the one-dimensional Fractional Laplacian to model the different sub-regimes of anomalous diffusion.

4 Analysis Techniques

In this section, we discuss the techniques used for the statistical analysis of PK-4 data. Those include particle tracking, drift subtraction, and techniques for fitting functions to MSD plots and velocity/displacement histograms reconstructed from experimental data. The analysis codes used in this work are all open sourced and can be found at <https://github.com/IPL-Physics/Open-Source>.

4.1 Particle Tracking and Drift Subtraction

Here we consider PK-4 particle observation camera videos in which the laser sheet was fixed in the central region of the cloud for extended periods of time (about 20 s). The camera frame rate used was 71 *fps* resulting in a 0.014 s time step. The region of interest in the videos was a rectangular section in the center of each cloud with size 14 mm by 2 mm. The typical number of particles detected per frame was 470. This yields statistically significant datasets with 20k data points or more in each set. The particle positions in the xz-plane were obtained using the open source particle tracking Mosaic Suite plugin of Fiji, which is a distribution of ImageJ [68]. The dust positions were converted from pixels to μm assuming a pixel resolution of 14.20 μm [31]. The particle trajectories imported from ImageJ include trajectories that do not start at the same time and do not last for the same duration. As shorter tracks can correspond to particles that move in and out of the plane illuminated by the laser sheet, we discarded tracks where the particles appear in fewer than 10 frames (or 0.14 s). The remaining trajectory data were used as inputs in the `@msd_analyzer` code to subtract drift, compute MSDs, and construct histograms of particle displacements and velocities. The nine pressure-current cases considered here use identical particle tracking datasets as those in [61], which investigated the anisotropic structure of the PK-4 clouds using pair correlation analysis. Thus, we expect that the results obtained here and in [61] are directly comparable.

The open-sourced code `@msd_analyzer` [40] was used to analyze the data. The developers of `@msd_analyzer` also developed the Mosaic Suite in Fiji, providing good compatibility between the code and the particle tracking data to construct the MSD (with options to provide the standard deviation and check for localization error) and to create the histograms of dust displacements and velocities. The `@msd_analyzer` code was also used to calculate the velocity autocorrelation, detect directed motion, and subtract drift. Those steps were necessary to ensure that the statistical analysis is performed on the diffusion portion of the dust motion, subtracting convective motion. In addition, motion along the direction of the external electric field E (the x-axis or the \parallel – direction) is considered separately from motion across the the direction of E (the z-axis or the \perp – direction). This was necessary due to the anisotropic coupling of the dust particles discussed in [61].

Each PK-4 dataset used in our analysis was extracted from a large field of view, encompassing a large portion of the dust cloud. As a result, we could break up the field of view in to smaller sections and calculate different drifts in different domains or sections of the cloud. This was necessary as nonhomogeneous drift was observed for several datasets. To address this issue, a method of nonhomogeneous drift subtraction (NHDS) was developed. In this method, the large field of view is separated into 12 smaller regions, as shown in Figure 3 A, and homogeneous drift subtraction is performed for each region. The number of smaller regions was selected to balance accuracy in drift subtraction and reasonable computation times. The NHDS method was validated against cases where the normal homogeneous drift subtraction worked, such as the case at 70 Pa pressure and 0.7 mA dc current. We found the two methods produced the same results, with similar velocity auto-correlation and the total drift plots.

Figure 3 shows the case where the most pronounced nonhomogeneous drift was observed for 70 Pa pressure and 0.35 mA dc current. As can be seen in Fig. 3 B, in the presence of nonhomogeneous drift, applying the drift subtraction to the large region of interest produces particle trajectories that exhibit some coordinated motion (instead of showing random diffusive motion). The NHDS method seems to work better as shown in 3 C, though some small areas still exhibit coordinated motion instead of the desired diffusive behavior. The drifts for each smaller domain region are shown in 3 D. While the total drift simply implied that the dust particles were linearly drifting to the left, the domain drifts show a spread of drift directions.

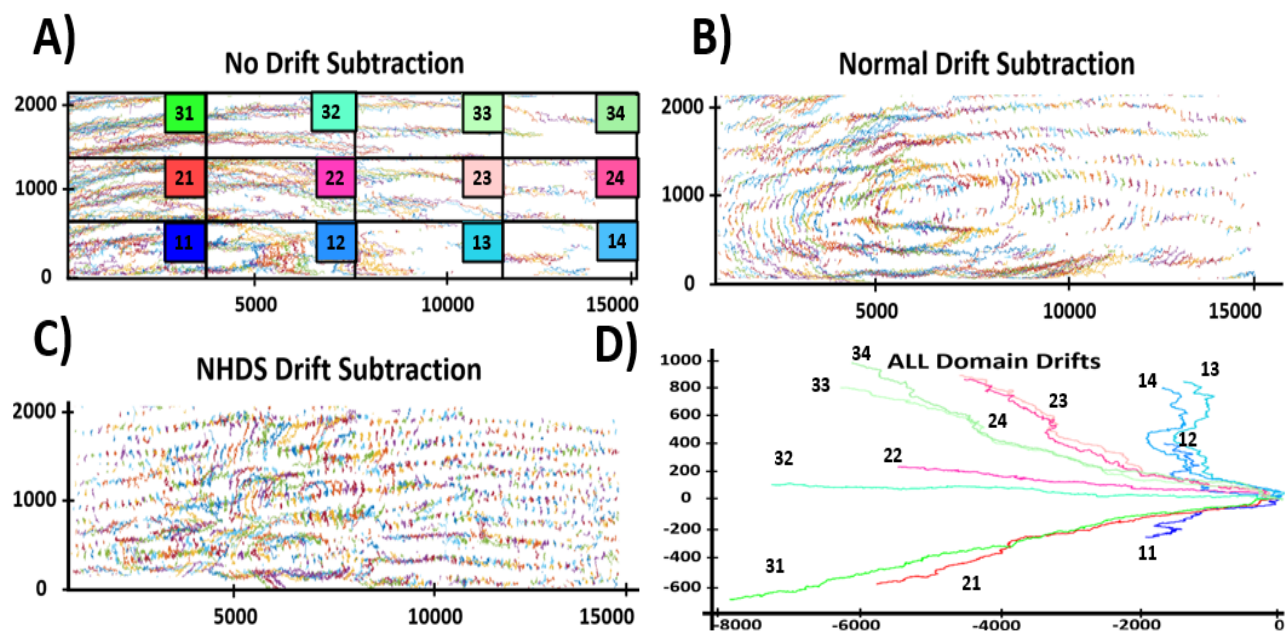


Figure 3: A) Dust particle tracks (μm) found using `@msdanalyzer` broken into 12 domains. B) Dust tracks (μm) after normal drift subtraction. C) Dust tracks (μm) after nonhomogeneous drift subtraction (NHDS). D) Average drift trajectories found in each domain in A). Experimental conditions were 70 Pa 0.35 mA.

As a quantitative check of the NHDS application of drift correction for the 70 Pa 0.35 mA case, we calculated the velocity autocorrelation of all domains before and after, shown in Fig. 4. While the velocity autocorrelation before subtraction (red) showed a nonzero value, after the NHDS subtraction (blue), the total autocorrelation dropped to zero. Using these drift-subtracted particle trajectories, we proceeded to find the values of α from a fit to the MHS plots and the values of q_p and q_v from fits to the position and velocity histograms. The values of α obtained from fits to the MSD plots at time delay of five seconds are very similar for two drift subtraction methods. However, the application of the NHDS method decreased the magnitude of the measured MSD (reflected in the vertical axis) by an order of magnitude.

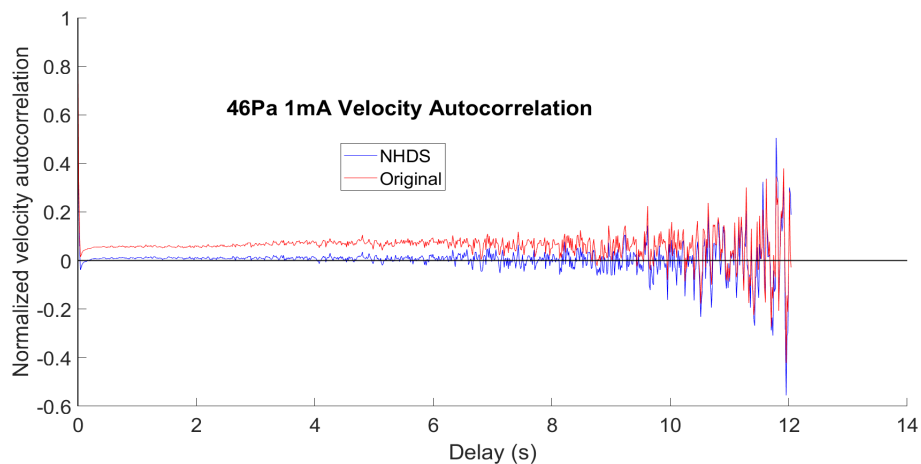


Figure 4: Velocity Autocorrelation of the 70 Pa 0.35 mA case before (red) and after NHDS (blue).

4.2 Fitting Techniques

In-house codes were developed to obtain nonlinear fits to the MSDs at different time delay intervals τ and distribution fits to the histograms. Fits to the displacement and velocity histograms were obtained using a Maxwellian (Eq. 9), a single q-Gaussian, and a Bi-q-Gaussian distributions of the form

$$\frac{A}{\sqrt{\pi v_{th}^2}} \left[1 + (q_v - 1) \frac{(v - v_0)^2}{v_{th}^2} \right]^{\frac{-1}{q_v - 1}} \quad 1 \leq q_v < 3 \quad (11)$$

$$\begin{aligned} & \frac{A}{\sqrt{\pi v_{th1}^2}} \left[1 + (q_{v1} - 1) \frac{(v - v_0)^2}{v_{th1}^2} \right]^{\frac{-1}{q_{v1} - 1}} \\ & + \frac{A}{\sqrt{\pi v_{th2}^2}} \left[1 + (q_{v2} - 1) \frac{(v - v_0)^2}{v_{th2}^2} \right]^{\frac{-1}{q_{v2} - 1}} \quad 1 \leq q_{v1, v2} < 3. \end{aligned} \quad (12)$$

Here A , v_{th} , v_0 , and q are the fitting parameters for the velocity histograms. The fits to the position histograms used the same distributions where v_{th} was replaced by D and $(v_r - v_{r0})^2$ was replaced by $(r(\tau) - r_0)^2$. To minimize fitting errors, the normalization in Eq. 6 was set to 1. Dropping this normalization has a negligible effect. For all cases, it was found that the axial component of the velocities (displacements) is best approximated by a single q-Gaussian, while the radial component was best approximated by a Bi-q-Gaussian. The value of q found from the position and velocity histogram fits are denoted as q_p and q_v , respectively. Data obtained from particle displacements/velocities along the axial direction is labeled by a subscript \parallel , while cross-field direction data have a subscript \perp .

5 Results

In this section, the MSD exponents α and nonextensive parameters q_p and q_v are given subscripts corresponding to the directions parallel and perpendicular to the electric field in the PK-4 experiment. The cross-field position histograms are best approximated by Bi-q-Gaussian with a mostly Gaussian "sub-population" ($q_{\perp 1} \approx 1$) and a 'halo-tail' ($q_{\perp 2} > 1$). Table 2 provides the fitted parameters α , q_p , and q_v quantifying anomalous diffusion and nonequilibrium in the parallel and perpendicular direction for the different pressure-current cases.

Pressure-Current		α_{\parallel}	α_{\perp}	$q_{p\parallel}$	$q_{p\perp 1}$	$q_{p\perp 2}$	$q_{v\parallel}$	$q_{v\perp 1}$	$q_{v\perp 2}$
70 Pa	1 mA	2.01	1.05	1.81	1.40	1.60	1.14	1.20	2.21
	0.7 mA	1.68	1.13	1.70	0.98	1.25	1.13	1.30	1.63
	0.35 mA	2.05	1.45	1.55	0.96	1.38	1.17	1.23	1.38
46 Pa	1 mA	2.40	0.925	1.44	0.98	1.27	1.31	1.12	2.12
	0.7 mA	1.54	1.10	1.41	0.95	1.20	1.24	1.27	1.82
	0.35 mA	2.03	1.40	1.47	0.95	1.21	1.18	1.17	1.60
30 Pa	1 mA	1.68	1.18	1.33	0.99	1.22	1.41	1.22	2.10
	0.7 mA	1.50	1.04	1.25	0.94	1.28	1.28	1.11	2.31
	0.35 mA	1.67	0.88	1.34	1.07	1.10	1.23	1.19	1.60

Table 2: Values α from MSD, q_p from displacement histogram, and q_v from velocity histogram for each of the nine sets of pressure-current conditions.

5.1 Fits to MSD Plots

Figure 5 shows the MSD plots obtained from dust positions within a 2D plane for all cases after drift subtraction. A nonhomogeneous drift subtraction was necessary for the two of the cases: (70 Pa, 0.35 mA) and (46 Pa, 1 mA). For all three pressure cases, it seems like highest current (1 mA) leads to the largest slope of the MSD plots, suggesting an enhanced superdiffusive behavior (see dark red, dark blue, and dark green line on the plot). Normally, in the presence of linear drift in the dust motion, the MSD plot will resemble superdiffusivity. An increased dc current is expected to result in an increased electric field strength which would enhance the drift of all charged particles. However, in this case, the fast switching of the dc polarity should still prevent dust response. In addition, examination of the velocity autocorrelation suggests that drift has been successfully subtracted from the particles trajectories, leaving only random motion. Thus, it is likely that the engaged superdiffusive trend is related to the effect that dc current has on the ion stream velocity, charge on the dust, and the resulting ion wakefield structure surrounding each dust particle.

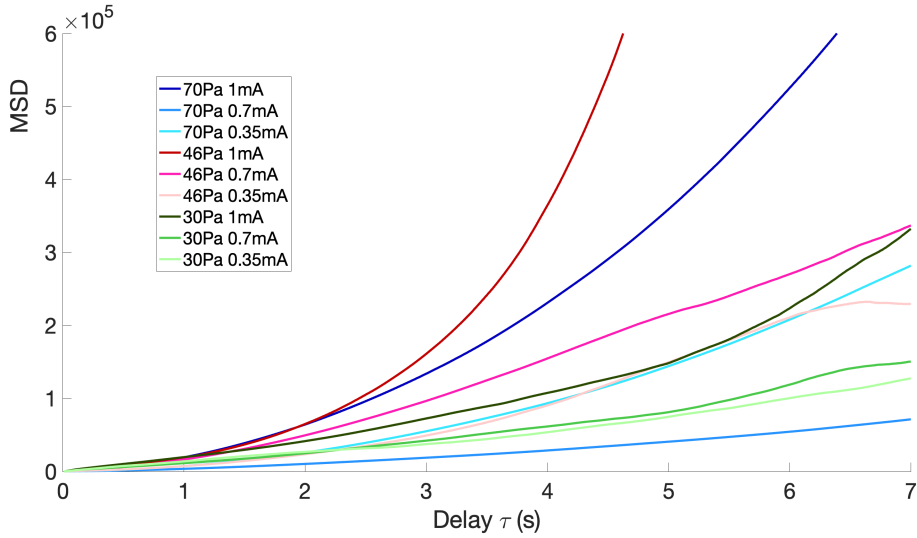


Figure 5: MSD plots for all cases after drift subtraction zoomed in to help distinguish different curves. The y-axis is the mean squared displacement ($\mu m^2/s$) and the x-axis is time delay in seconds.

To better understand the role of directional anisotropy, we calculated MSDs from particle displacements along \parallel and across \perp the direction of the external electric field. Separate fits were performed at different time delays to assess the role of distinct physical processes. Only data corresponding to time delays smaller than 10s was used for the fits. At larger time delays, the standard deviation from the mean MSD increases considerably due to decreasing number of data points. Figure 5 shows representative plots of MSD_{\parallel} and MSD_{\perp} for the 70Pa, 1mA case. For all pressure-current conditions the MSD_{\parallel} has a magnitude much greater than MSD_{\perp} and the plots of MSD_{\parallel} look almost identical to those of the combined MSDs in Fig. 5. The MSD_{\parallel} for all conditions has a positive concavity at all time delays, suggesting superdiffusion. The one exception is the (30 Pa, 0.35 mA) case, which has a brief negative concavity at its start. This dataset had the most noisy trajectories and the least number of data points at long time delays. Thus, the deviation in observed behavior may be due to the poorer quality of the data. The MSD_{\perp} for all cases exhibits a brief negative concavity for a delay period of about two seconds, followed by a positive concavity at larger time scales. This suggests that there may be a trapping mechanism causing sub-diffusive behavior at time scales smaller than 2s. These effects are showcased in the plots in Fig 6.

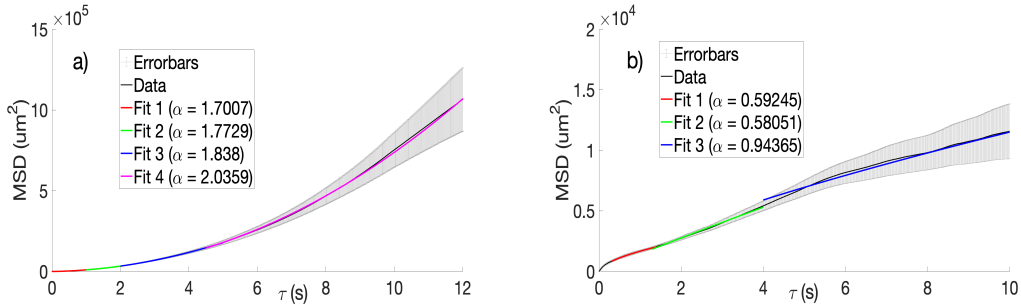


Figure 6: Fits to mean square displacement for different time delays for the 70Pa, 1mA case. a) MSD plot representative of the axial motion and b) MSD plot representative of the radial motion. The scale of the y axis differ by an order of magnitude between a) and b). This is that more the 2D diffusion is dominated by the axial direction.

Figure 6 is representative of the MSD curves in the parallel and perpendicular directions across all the pressure-current cases. Key features to notice are the larger y-axis scale for the parallel case, the

distinct superdiffusive $\alpha > 1$ curve for the parallel direction, and subdiffusive $0.1 < \tau < 1$ to linear shape ($\tau > 5$) of the perpendicular direction. These are consistent across all pressure-current cases.

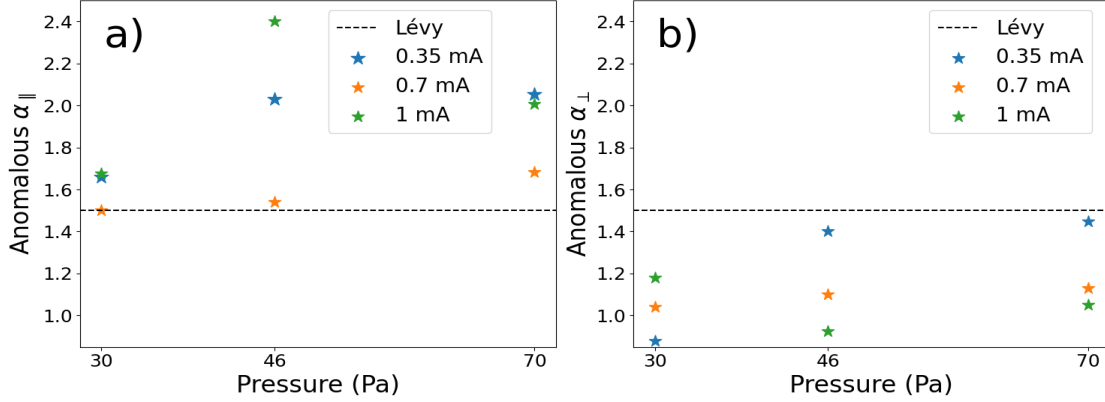


Figure 7: α_{\parallel} and α_{\perp} for all pressure-current cases.

The exponent α extracted from MSD_{\parallel} and MSD_{\perp} at time delay between 4 s and 5 s is plotted for all cases in Fig. 7. This time period was chosen as it has the most consistent slope fitting while not being too short of a time delay. Recall that Tsallis' theory claims that the diffusion is a Lévy process when $q > 5/3$. Using the scaling relation $MSD = \langle r^2 \rangle \propto \tau^{\frac{2}{3-q_p}}$ [63] yields the criterion $\alpha > 3/2$ for a Lévy process. Note that this scaling is valid only for q_p obtained from the displacement distributions. A dashed line on Fig. 7 marks the location of $\alpha = 3/2$, indicating that almost all distributions for the parallel cases are a Lévy processes, while the perpendicular direction are not. Later we compare this value of α to that found from q_p .

5.2 Fits to Displacement Histograms

Representative histograms of the displacements are shown in Fig. 9 for 70 Pa 0.7 mA case. The histograms of displacements parallel to the electric field are best approximated by a single q-Gaussian distribution, while the histograms of cross-field displacements are best approximated by a Bi-q-Gaussian distribution in most cases. These are displacements of all particles at time delay $\tau = 5$. The directional difference of the distributions type implies there is anisotropic diffusion. The nonextensive q_p parameters extracted from the displacement histograms are plotted in Figure 8.

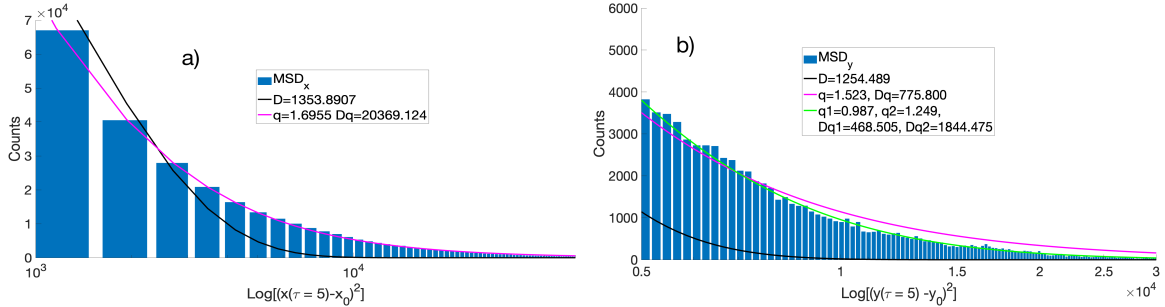


Figure 8: Position distribution fit example from case 70 Pa 0.7 mA for displacements in a) parallel direction and b) cross field direction plotted in logarithmic scale. The data for the position distributions is the positive squared value of $(r(\tau) - r_0)^2$ instead of the velocity distributions v_r . Since the data of $(r(\tau) - r_0)^2$ is already squared we fit it to a q-exponential instead of a q-Gaussian.

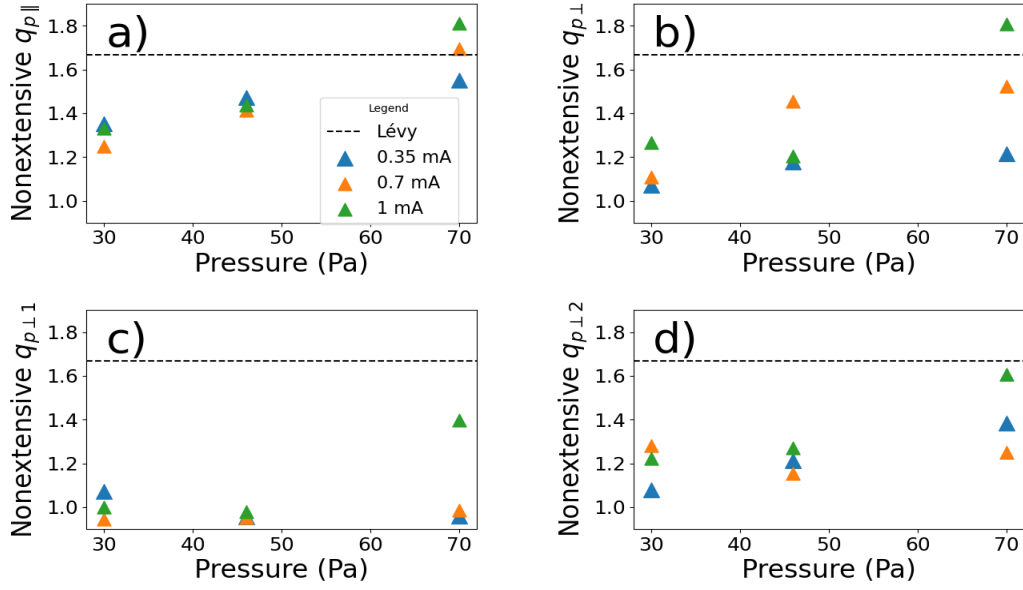


Figure 9: Coefficients extracted from nonextensive q_p fits : a) parallel $q_{p||}$, b) perpendicular single q-Gaussian $q_{p\perp}$, c) perpendicular from Bi-q-Gaussian with Gaussian-like sub-population $q_{p\perp 1}$, and d) perpendicular 'tail-halo' $q_{p\perp 2}$.

Notice that the coefficients for the parallel direction are again larger than for the perpendicular direction. Dashed line indicates a Lévy process. The coefficients extracted from the histogram of parallel displacements suggest that two of the 70Pa cases are consistent with a Lévy process. A crossover to a Lévy process is also seen for the cross-field direction in the 70 Pa, 1mA case if a single q-Gaussian is fitted to the histogram of cross-field displacements. However, the more accurate Bi-q-Gaussian fit to the cross-field displacement histograms suggest that the process is likely superdiffusive but not Lévy. These results are in qualitative agreement with the conclusions drawn from the α coefficients extracted from the MSD fits at time delay $\tau = 5$ shown in Figure 7. It seems that higher pressures create larger spread in the coefficients and exhibit a larger difference between the parallel and perpendicular directions suggesting a more pronounced anisotropic effect. The values for the diffusion $D \left(\frac{\mu m^2}{s} \right)$ calculated from Eq. 10, are shown in Fig. 10. Here we can see that, in the direction parallel to the field, an increase in pressure causes diffusion to increase. However, in the cross-field direction, the interpretation is less straightforward. $D_{\perp 1}$ and D_{\perp} generally decrease with pressure with some exceptions. $D_{\perp 2}$ does not show a clear trend with pressure or current.

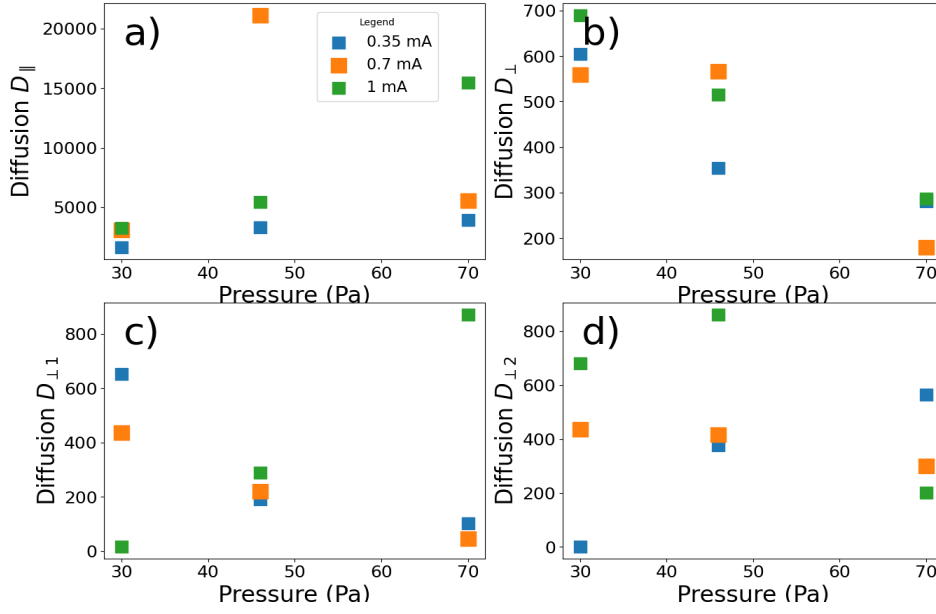


Figure 10: Diffusion coefficients ($/\mu\text{m}^2/\text{s}$) obtained from fits to the displacement histogram using q-Gaussian and Bi-q-Gaussian. a) parallel, b) perpendicular, c) perpendicular from Gaussian-like sub-population, and d) perpendicular from ‘tail-halo’ population.

Next, we examined how the exponent α found directly from MSD fits compares to α calculated from the displacement histogram fits using the scaling in Eq. 7. Figure 11 shows the percent difference $\frac{\alpha_{MSD} - \alpha_{qp}}{\alpha_{qp}}$. We can see that on average the error is lower, indicated by the dashed line at 20%, for the cases where a Bi-q-Gaussian fit was used rather than a single q-Gaussian. This seems to be in agreement with findings from [30, 14].

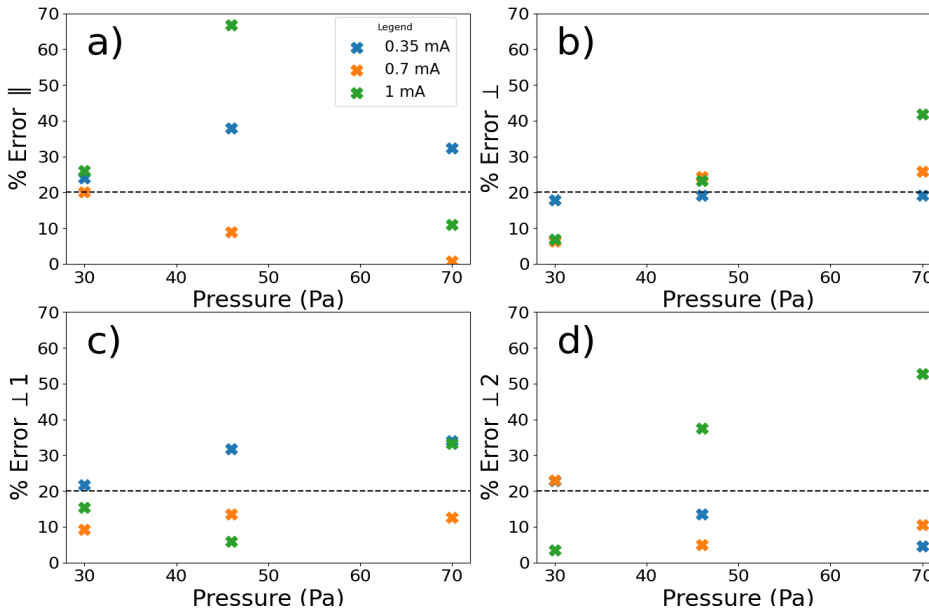


Figure 11: Percent difference between α found from MSD curves and α found from q_p using Eq. 7. a) parallel component, b) perpendicular component from a single q-Gaussian, c) Gaussian-like ‘sub-population’, and d) ‘tail-halo’. A dashed line at 20% is used to help compare the figures.

5.3 Velocity Distribution Plots

Next we examine Fig. 12, which shows representative histograms and distribution fits for the velocity components parallel and perpendicular to the direction of the external electric field. These plots show that a Gaussian or a Maxwellian distribution (black line) does not approximate the ‘fat’ tails of the histograms, while a q-Gaussian (magenta line) and a Bi-q-Gaussian (green line) provide good fits to the \parallel and the \perp velocity histograms, respectively. It is again observed that the distribution features change substantially with direction, suggesting anisotropic dust diffusion caused by the external electric field. Similar to the displacement data, we observe that the velocity histograms in the cross-field direction are best approximated by a Bi-q-Gaussian fit, suggesting a superposition of two distinct diffusion processes. These trends in histogram shapes are observed for all pressure-current cases. This will be further discussed in Sec. 6.2.

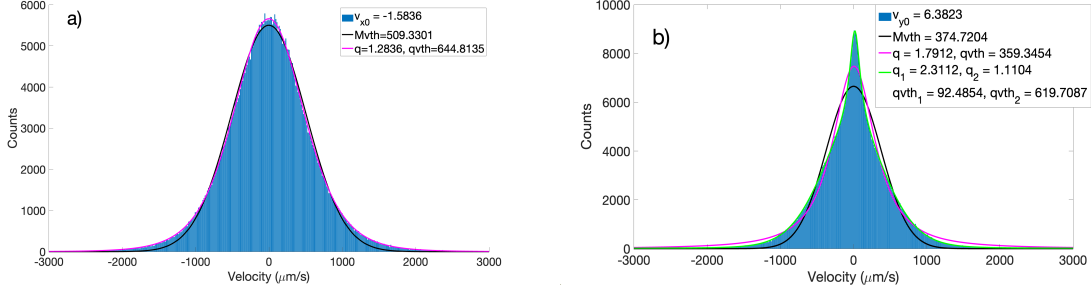


Figure 12: Velocity component histograms and distribution fits for the 30 Pa, 0.7mA case. a) Velocity components along the direction of the electric field. b) Velocity components in the cross-field direction.

Figure 13 shows the parallel and perpendicular nonextensive q parameters obtained from the velocity histograms for each pressure-current case. A slight negative slope is observed for increasing pressure for $q_{v\parallel}$ and none of the coefficients are above the Lévy line. The single q-Gaussian fits for the cross field velocity histograms had an $R^2 = 0.973$ and a normalized root mean square error $NRMSE = 0.027$ while the Bi-q-Gaussian fit had $R^2 = 0.993$ and $NRMSE = 0.013$. A larger value of R^2 and lower value of $NRMSE$ imply better fit thus the single q-Gaussian fits for the cross field velocity histograms are not as representative of the system as well as the Bi-q-Gaussian. With the Bi-q-Gaussian fits the $q_{\perp 1}$ values show little change with plasma conditions (most of them are around 1.2), while $q_{\perp 2}$ values seem to decrease with increasing pressure, except for the 1 mA case. The parameter q_v provides information on the equilibrium of the system, suggesting that in the direction parallel to the electric field, the dust ensemble is close to an equilibrium as seen in Figure 13 a), despite the strong superdiffusion observed in Figure 9 a). The trends in the cross-field direction are opposite, suggesting that the identification of the two distinct diffusion patterns drive the system away from equilibrium. This will be further discussed in Sec. 6.3.

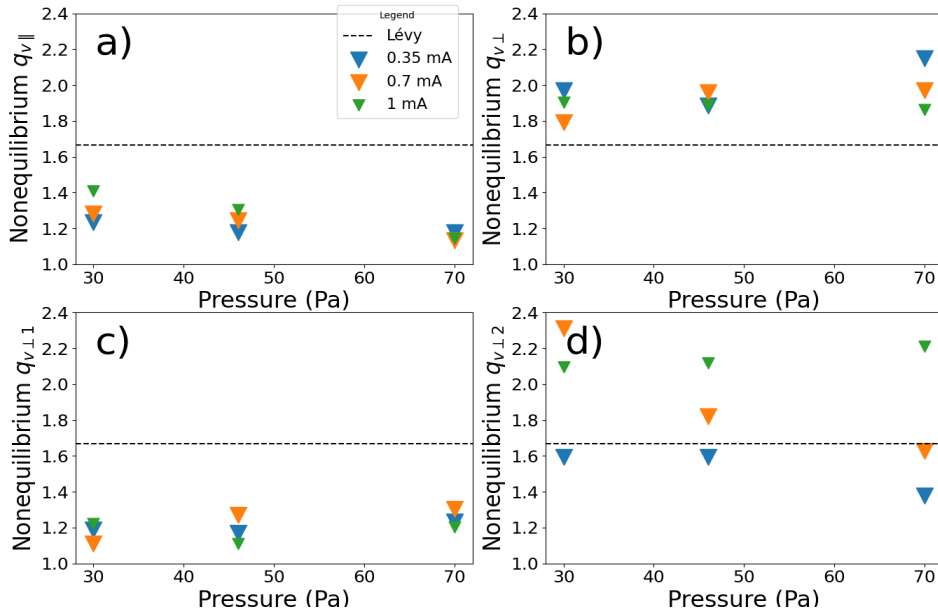


Figure 13: Nonequilibrium coefficients extracted from fits to velocity histograms for all pressure-current cases. a) $q_{v\parallel}$, b) single q-Gaussian $q_{v\perp}$, c) $q_{v\perp 1}$ is a Gaussian-like sub-population, and d) $q_{v\perp 2}$ is a 'halo-tail'.

The velocity distribution fits were used to extract dust temperatures for the directions parallel and perpendicular to the electric field. Figures 14 and 15 shows the temperatures found using a Maxwellian fit, and a q-Gaussian fit, respectively.

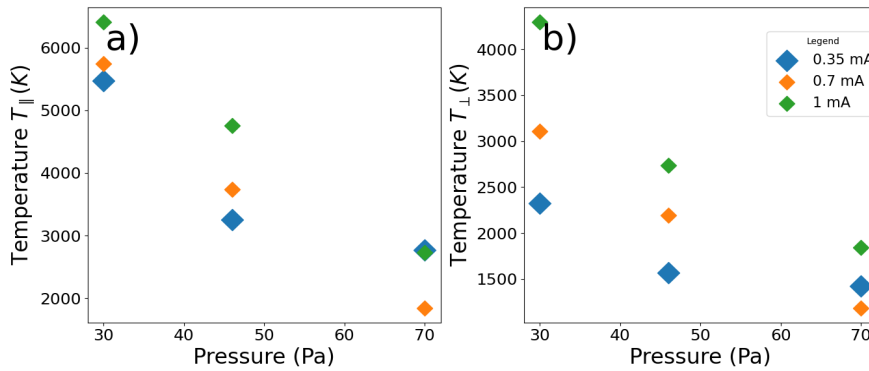


Figure 14: Temperatures for all pressure-current cases found using a Maxwellian fit to the a) parallel and b) perpendicular components of the velocity histograms.

Kinetic temperature is typically defined as the variance of a Maxwellian distribution. Since the velocity histograms for the dust in the PK-4 experiment are best approximated by a non-Maxwellian, the notion of "temperature" here is not well defined. The range of kinetic temperatures found from the Maxwellian fits (Fig. 14) is $2000K - 6500K$, or about $0.2eV - 0.6eV$, suggesting that the majority of the dust particles have very high kinetic energy even though the experiment is at room temperature and the pressure is low. Anomalously high dust temperature is a known phenomena that is caused by electrostatic fluctuations [69]. In Fig. 15, we used Eq. 10, $T_q(\frac{5q-3}{2}) = T_{Mq}$ (from [56]), since it provides a relation between the temperature or thermal velocity found from a q-Gaussian and to a 'Maxwellian-like' temperature.

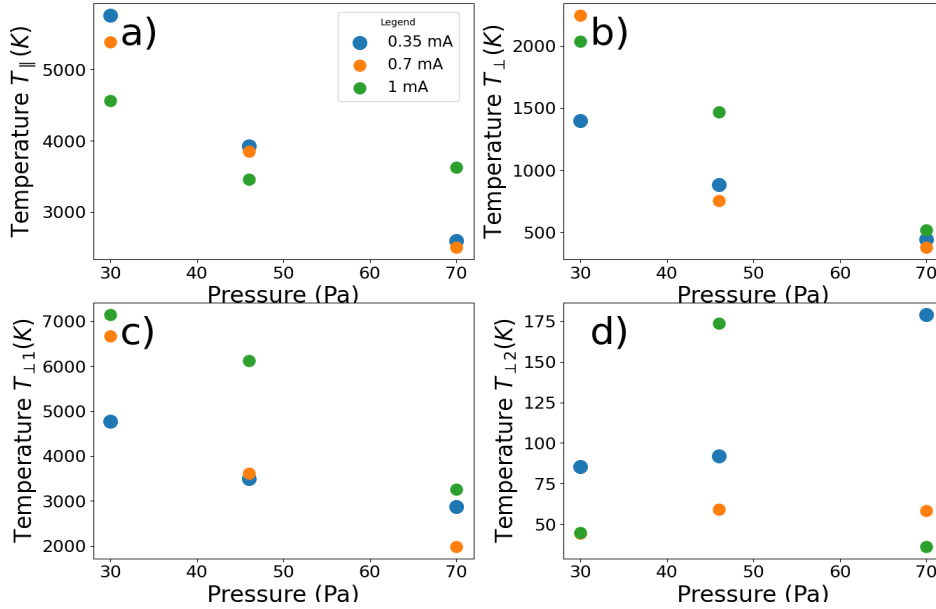


Figure 15: Temperatures T_{Mq} for all pressure-current cases found using non-Maxwellian fits to the parallel and perpendicular components of the velocity histograms. Temperature in the parallel direction a) was obtained using a single q-Gaussian fit. Temperatures in the perpendicular direction was found using a q-Gaussian b) and a Bi-q-Gaussian with a Gaussian-like sub-population fit c) and perpendicular ‘tail-halo’ fit d).

As shown in Figure 12 b), the perpendicular velocity histograms are best approximated by a Bi-q-Gaussian fit, where the the bulk distribution (the one with the larger variance and smaller q_v value) more closely resembles a Gaussian and, thus, can be used to extract the thermal velocity. The second distribution in the Bi-q-Gaussian accounts for the "fat tails". Thus, in Fig. 15, $T_{\perp 1}$ is extracted from a Gaussian-like sub-population distribution, while $T_{\perp 2}$ is obtained from fitting to a ‘tail-halo’ distribution. It may seem unintuitive why the Gaussian sub-population would have higher temperature values, while the ‘halo-tails’ have lower temperature values. This will be discussed in 6.2. Essentially we convert a variance from a distribution which has some ‘tailed-ness’ to a variance which does not have any, so that we can use the same definition of temperature. We argue that this is not a different treatment of temperature in dusty plasma, but an attempt at calculating temperature more carefully with nonextensive statistics. This allows us to derive more accurate dust temperatures for the PK-4 dusty plasma with values in the range $2500K - 5500K$, or about $0.2eV - 0.5eV$, which is smaller than the typically calculated values of $10 - 300eV$ [69].

Finally, for velocity q-distributions, Jiulin and Haining [70, 71] have derived the following expression for q_v in terms of a thermophoretic force and Lorentz force

$$q_v = 1 - \frac{k_B}{e} \frac{\nabla T_s}{(\nabla \phi + \vec{v} \times \vec{B})}. \quad (13)$$

T_s is the temperature for each species: electron, ion, or dust. In the PK-4, there is no magnetic field, thus, $\vec{v} \times \vec{B} = 0$. In the absence of a temperature gradient, $q_v = 1$ and the system is in equilibrium, i.e., the velocity histograms should be best described by a Maxwell-Boltzmann distribution. Equation 13 has not yet been verified against any experimental measurements, though we will give a qualitative argument for its possible credibility.

5.4 Domain Velocity Distribution Plots

Here we provide physical arguments why the Bi-q-Gaussian fit for the perpendicular histograms is needed. First, we consider the domain separation on Fig. 3 A) which was made for the NHDS method and reconstruct the velocity histogram in each domain. Figure 16 shows the velocity distribution for

domain 11 (dark blue in Fig. 3 A) in both the parallel and perpendicular directions for from the 30 Pa 0.7 mA case.

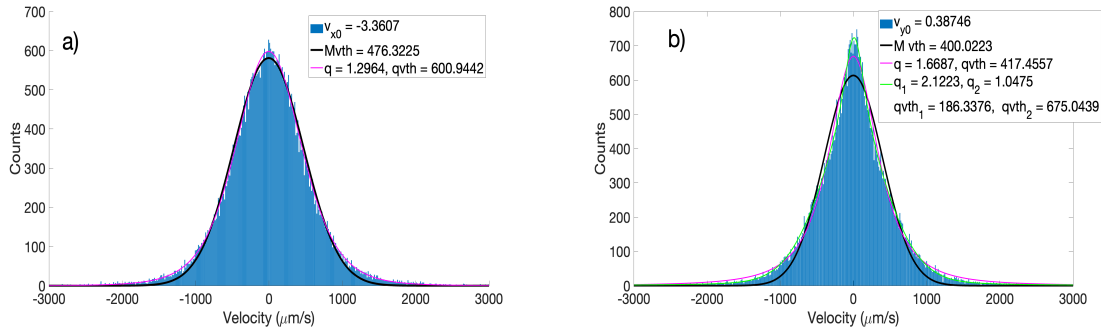


Figure 16: Velocity distributions for a) \parallel and b) \perp directions obtained from histogram fits of domain 11 for the case 30 Pa 0.7 mA. Notice that the q-Gaussian (magenta) curve provides a much closer fit than the one shown in Figure 12.

Although the Maxwellian fit still underpredicts the tails of the distribution, the single q-Gaussian fits the perpendicular histogram data much more closely than in Figure 12, though the Bi-q-Gaussian is also a reasonable fit. This phenomenon is apparent in all of the other domains and for all pressure cases with current 0.7mA . Other current cases were not analyzed. We attribute these differences to the transition between local and global dynamics as the system size increases. The nonextensive Tsallis parameter can be used to assess the nonequilibrium state of the system with equilibrium represented by $q = 1$ and nonequilibrium by $q \neq 1$. The different local domains in a system may be more or less in equilibrium depending on the properties of the corresponding local distribution functions. As the sample of velocities used to create the histogram is increased to include multiple domains with varying equilibrium properties, the conclusions about global diffusion and thermodynamics may be significantly altered by the averaging process. A smaller domain size is more likely to provide accurate information on the nonextensive parameter q_v , whether the particles in the small region are in equilibrium or not. Of course, this requires that the number of data points in the smaller domain is sufficient to yield statistically significant results. Table 3 provides the values of all the nonequilibrium q_v parameters in each domain with each table entry representing the domain location in the field of view of the particle tracks, (Figure 3 A). This yields a spatial map of the equilibrium properties at different pressure of the PK-4 dust cloud. Table 3 shows that regions near the outer part of the dust cloud are typically further away from equilibrium than regions within the central region.

Nonequilibrium $q_{v\perp}$ in each domain

1.57	1.63	1.47	1.45
1.51	1.51	1.45	1.44
1.66	1.71	1.79	1.55

30 Pa 0.7 mA

1.98	2.05	2.01	1.83
1.63	1.68	1.68	1.58
1.63	1.66	1.62	1.60

46 Pa 0.7 mA

1.57	1.63	1.47	1.45
1.51	1.51	1.45	1.44
1.66	1.71	1.79	1.55

70 Pa 0.7 mA

3: The three tables show q_v placed in the table at the corresponding domain showing a spatial map of the equilibrium.

We use the newly-founded q-Gaussian fits to calculate temperature in each domain using Eq. 10. Figure 17 a) T_{\parallel} and b) T_{\perp} show temperatures in units of Kelvin for 20 domains calculated for the 30 Pa 0.7 mA case. Each domain contained about 500 dust tracks, a minimum of 10 time frames per trajectory, which yields statistically significant amount of data for the velocity fits. The data indicates that temperatures gradients exist in the PK4 system. As seen from Eq. 13, the temperature gradient and the gradient in potential are related through the q_v parameter. MD simulations of ions and dust in the PK-4, with conditions closely resembling the 70 Pa 0.7 mA case, reveal gradients in the electric potential surrounding each dust particles, as shown in Fig. 18 [38]. Examination of Figures 17 and 18 suggests that the dust clouds in PK-4 exhibit both temperature and electric potential gradients, in addition to q-Gaussian velocity distribution functions. This provides a qualitative argument for applying Eq. 12, which is dependent on the ratio of the thermophoretic force over the electric field force. Providing a quantitative validation for Eq. 13 is beyond the scope of the present paper and will be explored in future work.

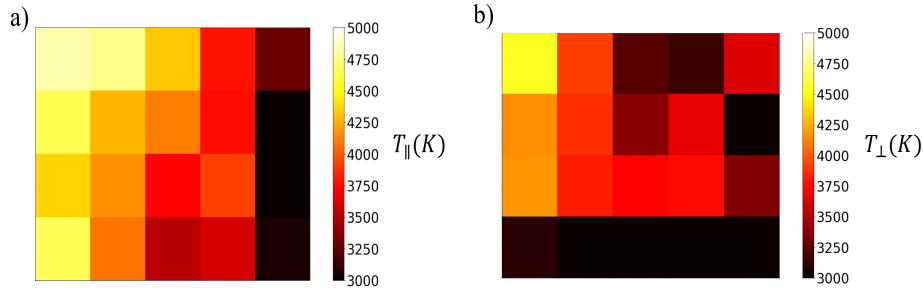


Figure 17: T_{\parallel} and T_{\perp} calculated in each domain showing temperature gradients (30 Pa 0.7 mA).

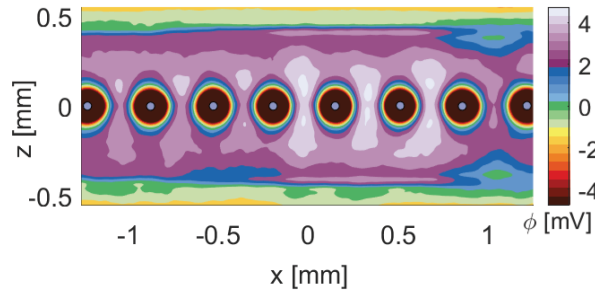


Figure 18: Electric potential in the vicinity of dust particles calculated by the DRIAD simulation. The simulation conditions closely reflect the 70 Pa 0.7 mA case.

6 Discussion

In this section, we compare of anomalous diffusion determined from fits to the MSD plots versus fits to the displacement histograms. We further discuss the possible physical mechanisms leading to the anisotropy observed when comparing the displacement and velocity distributions in the directions parallel and perpendicular to the electric field. Finally, we consider the nonequilibrium temperatures found from the velocity distribution fits.

6.1 MSD and Displacement Histograms

When analyzing the MSD plots fitting (Fig. 7), it seems like both α_{\parallel} and α_{\perp} increase with pressure for dc currents 0.35 mA and 0.7 mA. The trends are less obvious at 1 mA. These fits also indicate that none of the extracted α_{\perp} exponents correspond to a Lévy process, while all data for α_{\parallel} suggest a Lévy processes. Meanwhile, the q_p coefficients extracted from the position histogram fits (Fig. 9) also suggest that $q_{p\parallel}$ increases with pressure (i.e., enhanced superdiffusion), in agreement with the α_{\parallel} trends. However, only the highest pressure-currents case (70 Pa 1mA) in Fig. 9 indicates a Lévy processes (i.e., $q > 5/3$). The $q_{p\perp}$ values extracted from single q-Gaussian fits show similar trends for the same currents as α_{\perp} but the 70Pa 1mA case suggests a Lévy process, unlike α_{\perp} . The Bi-q-Gaussian fits yield $q_{p\perp 2}$ values that exhibit closer similarity to the α_{\perp} trends. We can also see from Figure 11 that the fits for $q_{p\perp 2}$ and $q_{p\perp 1}$ yield lower percent error between the predicted and measured α_{\perp} , strengthening the argument that the Bi-q-Gaussian is a more appropriate fit. The calculated diffusion constants (Fig. 10) show an overall increase in parallel diffusion with pressure, while the perpendicular diffusion seems to decrease with pressure when a single q-Gaussian fit is used. These trends are not as clear for $D_{\perp 1}$ and $D_{\perp 2}$ which were obtained from a Bi-q-Gaussian fit. Both the MSD fits and the displacement histogram fits indicate a pronounced difference in the diffusion regime when comparing the direction along the electric field versus the cross-field direction, which can be attributed to an anisotropy in the ion wake-mediated dust-dust interaction potential.

The statistical analysis suggests that at high pressure-current conditions, a transition from superdiffusion to a Lévy process is expected in the axial direction. In the cross-field direction, the Bi-q-Gaussian fits suggest that the observed behavior is a superposition of a classical diffusion and superdiffusion, but no crossover to Lévy process is expected. These observations can be explained when considering the physical mechanisms causing the dust particles in the PK-4 experiments to organize into field-aligned filamentary structures. The alignment and the strong coupling of dust grains along the direction of the electric field is caused by enhancement of the ion wakefield focusing and elongation of the wakefield structure surrounding the dust grains (as discussed in [38]). The formation of positive space charge due to ion focusing will cause a negatively charged dust grain to drift locally towards a nearby concentration of ions. This local drift is a nondeterministic microscopic effect, which is why it affects the microscopic motion by causing pronounced superdiffusion. The elongated ion wakefield structure surrounding the dust grains also causes a restoring force in the cross-field direction that keeps the individual dust particles aligned within the filament. This can explain the subdiffusive (or trapping) trends observed at small time scales in the cross-field MSD plots. Finally, if a dust particle escapes the confining potential that otherwise keeps it within a crystal-like filamentary structure, it cannot easily find force balance in between filaments. Instead, the dust particle makes large-scale jumps across the cloud until force balance is found within another filament. These jumps are frequently observed in video data from PK-4.

6.2 Histogram Shape in the Cross-field direction

Both the position and velocity histograms obtained for the \perp direction (Figure 8, 12) were best fit by a bimodal distribution, i.e., the complex shape of the distribution can be viewed as a superposition of two simpler distributions. The single q-Gaussian which yielded the best results and fewest errors in the parallel direction, does not fit well in the perpendicular direction. We concluded that a Bi-q-Gaussian provided the best fit. Liu and Goree [15] showed that the dust velocity histogram in the PK-4 experiments can be described by what they called a Maxwellian 'core' and a Kappa distribution 'halo',

$$f_{M+\kappa}(v) = Ae^{\frac{-v^2}{v_{th}^2}} + \frac{B}{(1 + \frac{v^2}{\kappa v_{th}^2})^\kappa}. \quad (14)$$

Equation 14 is very similar to the Bi-q-Gaussian as the Maxwellian 'core' is recovered by setting $q = 1$ for one of the q-Gaussian distributions, while the Kappa 'halo' is identical to the q-distribution when one uses the known scaling relation $q = 1 + 1/\kappa$ in the other q-Gaussian. In addition, Liu and Goree concluded that the cloud exhibited liquid-like coupling as evidenced by the calculated pair correlation function. The dust cloud in these experiments was confined in rf plasma produced by an rf coil and the observed cloud structure was homogeneous. In contrast, the present experiments were conducted in a pure dc discharge and the observed cloud structure was found to exhibit anisotropic coupling, suggesting both liquid and crystalline properties [61]. In both cases, the distributions consist of two terms, which implies a superposition of two distinct diffusion processes. Figure 19 shows a decomposition of the Bi-q-Gaussian into individual q-Gaussians.

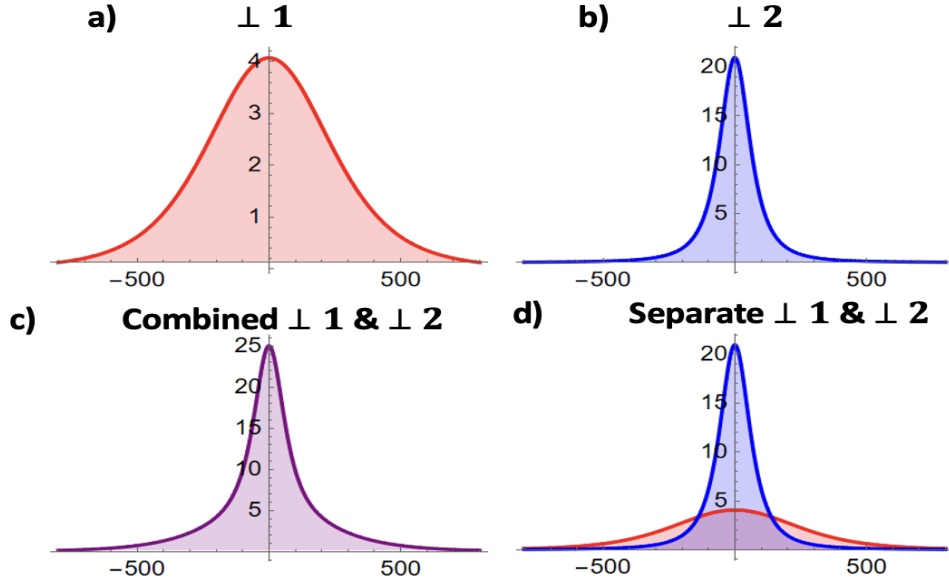


Figure 19: Components of the Bi-q-Gaussian illustrating two distinct populations: a) red $q_1 = 1.3$ and variance $\sigma_1 = 330$, while b) blue $q_2 = 1.63$ and $\sigma_2 = 63$. These are the same as the q_v values found for the cross-field velocity distribution in the 70 Pa 0.7 mA case.

The superposition of the two q-Gaussian distributions shown in Fig. 19 d) shows that one diffusion process (in red) is characterized by a small peak but large variance, while the other one (in blue) has both a large peak and large tails. The variance (and the corresponding temperature) of the blue distribution, however, is much smaller. Thus, the observed diffusion in the cross-field direction can be viewed as a superposition of two processes - one with higher temperature close to equilibrium and a second one with a lower temperature but farther from equilibrium.

This distribution shape is also called a 'knee and ankle' distribution, shown in Figure 20.

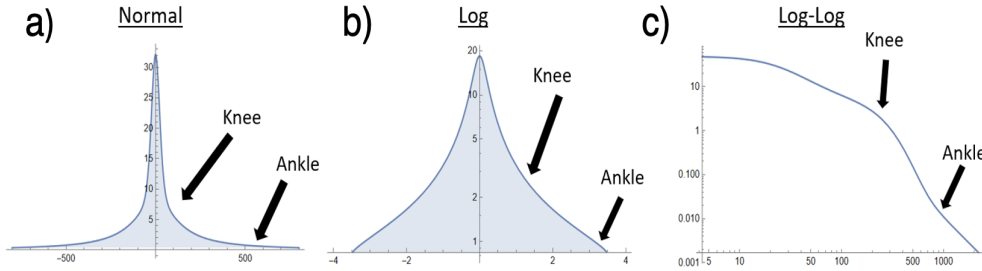


Figure 20: Analytical plot of the "knee and ankle" distribution a) with normal axis, b) a log scale, and c) log-log scale.

The 'knee and ankle' distribution has also been observed in solar wind ion and electron velocities and magnetic field fluctuations δB [72, 73, 74] as well as in fluxes of cosmic rays [75]. In [74], a bi-kappa distribution was proposed to explain the scale-dependent changes in the solar wind PDFs obtained from spacecraft measurements. It was pointed out that small scale PDFs are highly non-Maxwellian, while Maxwellian is recovered for large scales. In PK-4, the dust particles seem to exhibit similar disparity between small and large scales as evident from the distribution fits. As the dust diffusion is highly dependent on ion-wake-mediated interaction potential, small time fluctuations in the ion wakefield can be the reason for the highly non-Maxwellian features in the PDFs. Such fluctuations are expected to result from high-frequency ionization waves that were recently discovered in PK-4 [37].

In Space Physics, it is common to describe the non-Maxwellian velocity distributions using the kappa-distribution which is related to the q-Gaussian by $\kappa = \frac{1}{q-1}$. In [73], three physical mechanisms for generating a Kappa distribution were proposed: (i) Debye shielding, (ii) magnetic field binding, and (iii) temperature fluctuations. It was proposed that κ has a negative correlation with the Debye number N_D (number of particles in the Debye sphere). As κ is inversely related to q , we expect a positive correlation between N_D and q . In other words, increasing number of ions in the Debye spheres surrounding the dust should lead to enhancement of the superdiffusion. It was also proposed in [73] that κ is positively correlated with magnetic field fluctuations δB , which would imply negative correlation between q and δB . While there is no magnetic field in PK-4, the charged dust particles are aligned to the external electric field. Thus, we conjecture that increase in electric field fluctuations should randomize the dust motion, thus, leading to classical diffusion. Finally, the negative correlation between κ and the magnitude temperature fluctuations δT^2 proposed in [73] suggests a positive correlation between q and δT^2 . The role of temperature and temperature fluctuations in PK-4 will be further discussed in the next section. According to [76], the magnetic field fluctuations, δB , nearer the Sun around 6.9–9.7 AU, or even 43.6–47.2 AU, remain in a non-Gaussian, meta-equilibrium state. However, farther out between 80–87 AU, where the system has had more time (≈ 1 year) to relax, the magnetic field fluctuations reach a Gaussian distribution suggesting an equilibrium in magnetic field fluctuations. In other words, at these distances the solar-wind relaxes back to an equilibrium after going through a transition in the diffusion regime from $q > 5/3$ to $q < 5/3$ between ~ 47 AU and ~ 80 AU. Similar nonequilibrium-to-equilibrium regime transitions can be explored more easily and cost-effectively in laboratory settings with a dusty plasma experiment.

6.3 VDFs and Temperature

As shown in Fig. 15, temperature decreases with increasing pressure for T_{\parallel} and $T_{\perp 1}$, aligning with the conclusions presented in [61], where it was seen that dust 'cooled off' due to the increased role in dust neutral collision, which was calculated by use of pair-correlation functions. The temperatures $T_{\perp 2}$, however, seem to show the opposite trend of increasing with increased pressure. The Tsallis coefficients $q_{v\parallel}$, never exhibit values greater than $5/3$, which suggests that there is no Lévy processes for this direc-

tion. We also notice that $q_{v\parallel}$ tends to decrease with increasing pressure (thus, improving equilibrium), while increasing current slightly increases $q_{v\parallel}$ (thus, driving the system away from equilibrium). This is reasonable as an increase in pressure causes an increase in neutral collisions, meaning that the random collision process brings the dust motion to equilibrium. Meanwhile, the current provides an electric field which affects the ion streaming and focusing surrounding the dust, which can cause local attractive interactions among dust particles and macroscopic regions of positive space charge.

While the coefficients $q_{v\perp}$ and $q_{v\perp 2}$ suggest Lévy processes, the trends are not as simple to interpret. To visualize this, we look at Figure 19 a), which shows a hot population, more so in equilibrium, while the cold, shown in blue, has much lower kinetic energy. This is most likely due to the trapping potential that creates the observed filamentary structures within the dust cloud. However, the blue population is far from equilibrium. This population is confined in the cross-field direction and much of its kinetic energy is in the parallel direction. When this energy transitions to the cross-field direction, it may do so suddenly, resulting in the larger tails of the distribution, or big jumps of the dust particles in space. In other words, Figure 19 illustrates a one population that is highly peaked with significant tails (kurtosis), giving a small variance, i.e., temperature, and another distinct population that exhibits high variance but less kurtosis. Based on this interpretation, increasing pressure appears to drive the first population $q_{\perp 1}$ away from equilibrium, while improving equilibrium for the second population $q_{\perp 2}$ for all but the 1 mA case. The confining forces keep the dust particles in a crystal-like structure, mostly aligned in the parallel direction, but these forces do not always succeed in maintaining this configuration. Similar to slipping out between tight tweezers, particles that escape these confining forces become energetic in the perpendicular direction. Once the particles escape, their movement is primarily dictated by the ion wakefield caused by the electric field, leading to high parallel diffusion. In other words, the forces confining the dust must act in the parallel direction; otherwise, the particles would accelerate due to the electric field.

An examination of the domain velocity distributions at 0.7 mA reveals that $q_{v\perp}$ tends to be higher on the edges of the cloud and smaller in the center at low pressure, but larger on the top and smaller on the bottom for 46 Pa, 70 Pa. We also see that for 30 Pa at 0.7 mA there exist clear gradients in both the T_{\parallel} and T_{\perp} . (We remind the reader that there is only one T_{\perp} here since a single q-Gaussian fits well the individual domain data in the cross-field direction.) Unexpected high dust temperature has been a point of contention in the dusty plasma community because the experiments are always in a room temperature setting, however this is better understood when considering all forms of energy in strongly coupled systems. We propose that, in addition to the kinetic temperature of the dust, the additional apparent energy comes from variation of the electrostatic potential. Typically one calculates temperature as $E = k_B T = 1/2 m v_{th}^2$. However, we propose $E + U = k_B T + Q_{dust} \langle \Delta \phi_{float}^2 \rangle$, meaning that room temperature of the dust particles can be recovered by employing the following expression

$$T = \frac{1}{2} \frac{m}{k_B} v_{th}^2 - \frac{e}{k_B} \langle N_{dust} \rangle \langle \Delta \phi_{float}^2 \rangle. \quad (15)$$

An order of magnitude calculation using this equation reveals that variation in the floating electric potential on the order of 10^{-5} Volts could explain temperature discrepancy. This conclusion is explained more rigorously in [69].

7 Conclusions

The presented analysis of PK-4 dusty plasma experiments highlights the features of anomalous dust diffusion resulting from an interplay between temperature fluctuations and anisotropies in the dust-dust interaction potential caused by the application of external electric field to this strongly coupled complex system. Notably, we used non-extensive Tsallis statistics to quantify the nonequilibrium state of the system in the directions along and across the electric field using q-Gaussian distributions. The nonequilibrium parameters q_p and q_v (extracted from position and velocity distributions) have distinctly different values for the directions parallel and perpendicular to the electric field, as shown in Table 2. Particle motion parallel to the electric field is superdiffusive and for several pressure-current cases, superdiffusion crosses over to a Lévy process. In the cross-field direction, the diffusion is again anomalous, but the bi-Gaussian fit best describing the histograms suggests a superposition of two processes. One of

these processes is similar to a classical diffusion, while the other one is superdiffusive, but not Lévy. We attribute the directional dependence of diffusion to anisotropies in the dust-dust interaction potential and the dust temperature throughout the cloud. The former is caused by the anisotropic shape of the ion wakefield clouds surrounding the dust grains, which leads to the alignment of the dust particles into filaments. Inside a filament, macroscopic regions of positive space charge form along the direction of the electric field due to ion focusing causing local dust accelerations towards these attractors. Similarly, the cross-field motion of the dust is restrained due to a restoring force from the streaming ions within the wakefield structure. However, if a dust particle escapes the filament, it will experience large jumps across the cloud until it finds force balance within another filament (which is visible in the video data).

In addition, the kinetic temperature is found to vary throughout the dust cloud as shown in Fig. 17. Analysis of subdomains within the dust clouds reveals that a single q -Gaussian fit works well even in the cross-field direction for small domain sizes. Since the q_v extracted from velocity histograms quantifies the nonequilibrium state of the system, the domain analysis allows for a nuanced understanding of cloud properties, including the structural anisotropy, diffusion, and equilibrium state. Specifically, we conclude that the different domains within the same dust cloud are characterized by different diffusion regimes driving the global state away from equilibrium. Temperature gradients were identified for the dust in the PK-4. While all the temperatures were higher than room temperature, we propose that the observed high kinetic temperature is due to electrostatic fluctuations. Finally, we conclude that dusty plasma systems, such as those in PK-4, are excellent for studying nonequilibrium systems, anomalous diffusion and the physical origins of the two phenomena. As the mathematical description of these processes is universal, we expect that the dusty plasma experiments can be a practical means to investigate other nonequilibrium complex systems such as the solar wind.

8 Acknowledgments

This material is based on work supported by NSF grant numbers 2308742, 2308743, EPSCoR FTTP OIA2148653, 1903450, and 1740203, NASA grant number 80NSSC21K0381. All authors gratefully acknowledge the joint ESA - Roscosmos “Experiment Plasmakristall-4” onboard the International Space Station. The microgravity research is funded by the space administration of the Deutsches Zentrum für Luft- und Raumfahrt eV with funds from the federal ministry for economy and technology according to a resolution of the Deutscher Bundestag under Grants No. 50WM1441 and No. 50WM2044

References

- [1] P. K. Shukla. A survey of dusty plasma physics. *Physics of Plasmas*, 2001.
- [2] R. L. Merlino, J. R. Heinrich, S.-H. Hyun, and J. K. Meyer. Nonlinear dust acoustic waves and shocks. *Physics of Plasmas*, 19(5), March 2012.
- [3] S. A. Khrapak, B. A. Klumov, P. Huber, V. I. Molotkov, A. M. Lipaev, V. N. Naumkin, A. V. Ivlev, H. M. Thomas, M. Schwabe, G. E. Morfill, O. F. Petrov, V. E. Fortov, Yu. Malentschenko, and S. Volkov. Fluid-solid phase transitions in three-dimensional complex plasmas under microgravity conditions. *Physical Review E*, 2012.
- [4] American Physical Society. Made to order: Researchers discover a new form of crystalline matter. <https://phys.org/news/2015-11-crystalline.html>, 2015. Accessed: 2024-08-14.
- [5] Evdokiya G. Kostadinova, Emerson Gehr, Bradley Andrew, Lorin S. Matthews, Truell W. Hyde, and Abbie Terrell. Liquid plasma crystals on the iss. In *AIAA SCITECH 2023 Forum*. American Institute of Aeronautics and Astronautics, January 2023.
- [6] M. G. Hariprasad, P. Bandyopadhyay, V. S. Nikolaev, D. A. Kolotinskii, S. Arumugam, G. Arora, S. Singh, A. Sen, and A. V. Timofeev. Self-sustained non-equilibrium co-existence of fluid and solid states in a strongly coupled complex plasma system. *Scientific Reports*, 12(1), August 2022.

- [7] Alexei V. Ivlev, Philip C. Brandt, Gregor E. Morfill, Christoph Rath, Hubertus M. Thomas, Glenn Joyce, Vladimir E. Fortov, Andrey M. Lipaev, Vladimir I. Molotkov, and Oleg F. Petrov. Electrorheological Complex Plasmas. *IEEE Transactions on Plasma Science*, 38(4):733–740, April 2010. Conference Name: IEEE Transactions on Plasma Science.
- [8] Erasmus Experiment Archive. Complex plasma experiments with pk-4. <https://eea.spaceflight.esa.int/portal/exp/?id=9341>, 2012. Accessed: 2024-08-14.
- [9] V. N. Tsytovich, U. De Angelis, R. Bingham, and D. Resendes. Long-range correlations in dusty plasmas. *Physics of Plasmas*, 1997.
- [10] B. Smith, J. Vasut, T. Hyde, L. Matthews, J. Reay, M. Cook, and J. Schmoke. Dusty plasma correlation function experiment. *Advances in Space Research*, 2004.
- [11] Matheus V Correia, Emerson J Freitas, Leonardo R E Cabral, and Clécio C de Souza Silva. Structural phases of classical 2d clusters with competing two-body and three-body interactions. *Journal of Physics: Condensed Matter*, 35(41):415404, July 2023.
- [12] Kashif Arshad, M. Lazar, Shahzad Mahmood, Aman-ur-Rehman, and S. Poedts. Kinetic study of electrostatic twisted waves instability in nonthermal dusty plasmas. *Physics of Plasmas*, 2017.
- [13] O. F. Petrov, V. E. Fortov, O. S. Vaulina, A. V. Chernyshev, S. N. Antipov, A. V. Gavrikov, and I. A. Shakhova. Experimental Study of Dusty Plasma Kinetics. *Physica Scripta*, 2005.
- [14] Bin Liu and J. Goree. Superdiffusion and Non-Gaussian Statistics in a Driven-Dissipative 2D Dusty Plasma. *Physical Review Letters*, 2008.
- [15] Bin Liu, J. Goree, M. Y. Pustynnik, H. M. Thomas, V. E. Fortov, A. M. Lipaev, A. D. Usachev, V. I. Molotkov, O. F. Petrov, and M. H. Thoma. Particle velocity distribution in a three-dimensional dusty plasma under microgravity conditions. *AIP Conference Proceedings*, 2018.
- [16] Yan Feng. *Microscopic dynamics in two-dimensional strongly-coupled dusty plasmas*. PhD thesis, The University of Iowa, 2010.
- [17] E. Joshi, M. Y. Pustynnik, M. H. Thoma, H. M. Thomas, and M. Schwabe. Recrystallization in string-fluid complex plasmas. *Physical Review Research*, 5(1), March 2023.
- [18] E. G. Kostadinova, R. Banka, J. L. Padgett, C. D. Liaw, L. S. Matthews, and T. W. Hyde. Fractional Laplacian spectral approach to turbulence in a dusty plasma monolayer. *Physics of Plasmas*, 2021.
- [19] Sachin Sharma, Rauoof Wani, Prabhakar Srivastav, Meenakshee Sharma, Sayak Bose, Yogesh Saxena, and Sanat Tiwari. Observation of kolmogorov turbulence due to multiscale vortices in dusty plasma experiments, 2024.
- [20] Mangilal Choudhary. A review on the vortex and coherent structures in dusty plasma medium, 2024.
- [21] M. S. Murillo. Strongly coupled plasma physics and high energy-density matter. *Physics of Plasmas*, 2004.
- [22] A. V. Ivlev, G. E. Morfill, H. M. Thomas, C. R ath, G. Joyce, P. Huber, R. Kompaneets, V. E. Fortov, A. M. Lipaev, V. I. Molotkov, T. Reiter, M. Turin, and P. Vinogradov. First Observation of Electrorheological Plasmas. *Physical Review Letters*, 100(9):095003, March 2008. Publisher: American Physical Society.
- [23] Christopher Dietz, Johannes Budak, Tobias Kamprich, Michael Kretschmer, and Markus H. Thoma. Phase transition in electrorheological plasmas. *Contributions to Plasma Physics*, 61(10):e202100079, 2021. _eprint: <https://onlinelibrary.wiley.com/doi/pdf/10.1002/ctpp.202100079>.

- [24] J. Beckers, J. Berndt, D. Block, M. Bonitz, P. J. Bruggeman, L. Couëdel, G. L. Delzanno, Y. Feng, R. Gopalakrishnan, F. Greiner, P. Hartmann, M. Horányi, H. Kersten, C. A. Knaepk, U. Konopka, U. Kortshagen, E. G. Kostadinova, E. Kovačević, S. I. Krasheninnikov, I. Mann, D. Mariotti, L. S. Matthews, A. Melzer, M. Mikikian, V. Nosenko, M. Y. Pustyl'nik, S. Ratynskaia, R. M. Sankaran, V. Schneider, E. J. Thimsen, E. Thomas, H. M. Thomas, P. Tolia, and M. van de Kerkhof. Physics and applications of dusty plasmas: The perspectives 2023. *Physics of Plasmas*, 30(12), December 2023.
- [25] Mangilal Choudhary. Perspective: dusty plasma experiments—a learning tool for physics graduate students. *European Journal of Physics*, 2021.
- [26] Robert Merlino. Dusty plasmas: from saturn’s rings to semiconductor processing devices. *Advances in Physics: X*, 6(1), January 2021.
- [27] E. G. Kostadinova, K. Busse, N. Ellis, J. Padgett, C. D. Liaw, L. S. Matthews, and T. W. Hyde. Delocalization in infinite disordered two-dimensional lattices of different geometry. *Physical Review B*, 2017.
- [28] E G Kostadinova, C D Liaw, L S Matthews, and T W Hyde. Physical interpretation of the spectral approach to delocalization in infinite disordered systems. *Materials Research Express*, December 2016.
- [29] E.G. Kostadinova, F. Guyton, A. Cameron, K. Busse, C. Liaw, L.S. Matthews, and T.W. Hyde. Transport properties of disordered two-dimensional complex plasma crystal. *Contributions to Plasma Physics*, February 2018.
- [30] Bin Liu, J. Goree, and Yan Feng. Non-Gaussian statistics and superdiffusion in a driven-dissipative dusty plasma. *Physical Review E*, 2008.
- [31] M. Y. Pustyl'nik, M. A. Fink, V. Nosenko, T. Antonova, T. Hagl, H. M. Thomas, A. V. Zobnin, A. M. Lipaev, A. D. Usachev, V. I. Molotkov, O. F. Petrov, V. E. Fortov, C. Rau, C. Deysenroth, S. Albrecht, M. Kretschmer, M. H. Thoma, G. E. Morfill, R. Seurig, A. Stettner, V. A. Alyamovskaya, A. Orr, E. Kufner, E. G. Lavrenko, G. I. Padalka, E. O. Serova, A. M. Samokutyayev, and S. Cristoforetti. Plasmakristall-4: New complex (dusty) plasma laboratory on board the International Space Station. *Review of Scientific Instruments*, September 2016.
- [32] V. N. Naumkin, D. I. Zhukhovitskii, A. M. Lipaev, A. V. Zobnin, A. D. Usachev, O. F. Petrov, H. M. Thomas, M. H. Thoma, O. I. Skripochka, and A. A. Ivanishin. Excitation of progressing dust ionization waves on pk-4 facility. *Physics of Plasmas*, 28(10), October 2021.
- [33] A. Mendoza, D. Jiménez Martí, L. S. Matthews, B. Rodríguez Saenz, P. Hartmann, E. Kostadinova, M. Rosenberg, and T. W. Hyde. Ion density waves driving the formation of filamentary dust structures, 2024.
- [34] J. Goree, Bin Liu, M. Y. Pustyl'nik, H. M. Thomas, V. E. Fortov, A. M. Lipaev, V. I. Molotkov, A. D. Usachev, O. F. Petrov, M. H. Thoma, E. Thomas, U. Konopka, and S. Prokopiev. Correlation and spectrum of dust acoustic waves in a radio-frequency plasma using pk-4 on the international space station. *Physics of Plasmas*, 27(12), December 2020.
- [35] Bin Liu, John Goree, M. Y. Pustyl'nik, H. M. Thomas, V. E. Fortov, A. M. Lipaev, A. D. Usachev, O. F. Petrov, A. V. Zobnin, and M. H. Thoma. Time-dependent shear motion in a strongly coupled dusty plasma in pk-4 on the international space station (iss). *IEEE Transactions on Plasma Science*, 49(9):2972–2978, September 2021.
- [36] Ronald H. Freeman. Lunar exosphere: Dust-in-plasma? dusty plasma? *Journal of Space Operations and Communicator*, 20(4), 2024.
- [37] Peter Hartmann, Marlene Rosenberg, Zoltan Juhasz, Lorin S Matthews, Dustin L Sanford, Katrina Vermillion, Jorge Carmona-Reyes, and Truell W Hyde. Ionization waves in the pk-4 direct current neon discharge. *Plasma Sources Science and Technology*, 29(11):115014, November 2020.

- [38] Katrina Vermillion, Dustin Sanford, Lorin Matthews, Peter Hartmann, Marlene Rosenberg, Evdokiya Kostadinova, Jorge Carmona-Reyes, Truell Hyde, Andrey M. Lipaev, Alexandr D. Usachev, Andrey V. Zobnin, Oleg F. Petrov, Markus H. Thoma, Mikhail Y. Pustyl'nik, Hubertus M. Thomas, and Alexey Ovchinin. Influence of temporal variations in plasma conditions on the electric potential near self-organized dust chains. *Physics of Plasmas*, 29(2), February 2022.
- [39] Katrina Vermillion, Abbie Terrell, Emerson Gehr, Evdokiya G. Kostadinova, Peter Hartmann, Lorin S. Matthews, and Truell W. Hyde. Numerical modeling of the plasmakristall-4 experiment on the iss. In *AIAA SCITECH 2023 Forum*. American Institute of Aeronautics and Astronautics, January 2023.
- [40] Nadine Tarantino, Jean-Yves Tinevez, Elizabeth Faris Crowell, Bertrand Boisson, Ricardo Henriques, Musa Mhlanga, Fabrice Agou, Alain Israël, and Emmanuel Laplantine. TNF and IL-1 exhibit distinct ubiquitin requirements for inducing NEMO–IKK supramolecular structures. *Journal of Cell Biology*, 2014.
- [41] Andy Reynolds. Liberating Lévy walk research from the shackles of optimal foraging. *Physics of Life Reviews*, 2015.
- [42] M. Benhamou. Lecture on the anomalous diffusion in Condensed Matter Physics. *Materials and Devices*, 2018.
- [43] Yan Feng, J. Goree, and Bin Liu. Identifying anomalous diffusion and melting in dusty plasmas. *Physical Review E*, 2010.
- [44] Fernando A. Oliveira, Rogelma M. S. Ferreira, Luciano C. Lapas, and Mendeli H. Vainstein. Anomalous Diffusion: A Basic Mechanism for the Evolution of Inhomogeneous Systems. *Frontiers in Physics*, 2019.
- [45] Karen E. Daniels, Christian Beck, and Eberhard Bodenschatz. Defect turbulence and generalized statistical mechanics. *Physica D: Nonlinear Phenomena*, June 2004.
- [46] A. M. Reynolds and M. Veneziani. Rotational dynamics of turbulence and Tsallis statistics. *Physics Letters A*, June 2004.
- [47] Urgur Tirnakli. AGING IN EARTHQUAKE MODELS Complexity, Metastability and Nonextensivity. *World Scientific*, 2005.
- [48] A. Y. Abul-Magd. Nonextensive random matrix theory approach to mixed regular-chaotic dynamics. *Physical Review E*, 2005. Publisher: American Physical Society.
- [49] K. Ivanova, H. N. Shirer, T. P. Ackerman, and E. E. Clothiaux. Dynamical model and nonextensive statistical mechanics of liquid water path fluctuations in stratus clouds. *Journal of Geophysical Research: Atmospheres*, 2007.
- [50] P. Douglas, S. Bergamini, and F. Renzoni. Tunable Tsallis Distributions in Dissipative Optical Lattices. *Physical Review Letters*, March 2006.
- [51] I. Bediaga, E. M. F. Curado, and J. M. de Miranda. A nonextensive thermodynamical equilibrium approach in hadrons. *Physica A: Statistical Mechanics and its Applications*, October 2000.
- [52] L. P. Karakatsanis, G. P. Pavlos, and M. N. Xenakis. Tsallis non-extensive statistics, intermittent turbulence, SOC and chaos in the solar plasma. part two: Solar flares dynamics. 392(18):3920–3944.
- [53] G. P. Pavlos, L. P. Karakatsanis, and M. N. Xenakis. Tsallis non-extensive statistics, intermittent turbulence, SOC and chaos in the solar plasma, part one: Sunspot dynamics. 391(24):6287–6319.
- [54] Danny Summers and Richard M. Thorne. The modified plasma dispersion function. *Physics of Fluids B: Plasma Physics*, 3(8):1835–1847, August 1991.
- [55] Zhipeng Liu, Liyan Liu, and Jiulin Du. A nonextensive approach for the instability of current-driven ion-acoustic waves in space plasmas. *Physics of Plasmas*, 16(7), July 2009.

- [56] Muhammad Bilal, Aman ur Rehman, Mushtaq Ahmad, Muhammad Ahsan Shahzad, Muhammad Sarfraz, and Shahzad Mahmood. Linear analysis of whistler mode instability in anisotropic q-nonextensive distributed plasmas: a numerical approach. *Physica Scripta*, 98(9):095607, August 2023.
- [57] Yue Wang and Jiulin Du. The collision frequencies in the plasmas with the power-law q-distributions in nonextensive statistics. 566:125623.
- [58] Jingyu Gong and Jiulin Du. Dust charging processes in the nonequilibrium dusty plasma with nonextensive power-law distribution. *Physics of Plasmas*, 19(2), February 2012.
- [59] Zhipeng Liu and Jiulin Du. Dust acoustic instability driven by drifting ions and electrons in the dust plasma with lorentzian kappa distribution. *Physics of Plasmas*, 16(12):123707, December 2009.
- [60] Johannes Schindelin, Ignacio Arganda-Carreras, Erwin Frise, Verena Kaynig, Mark Longair, Tobias Pietzsch, Stephan Preibisch, Curtis Rueden, Stephan Saalfeld, Benjamin Schmid, Jean-Yves Tinevez, Daniel James White, Volker Hartenstein, Kevin Eliceiri, Pavel Tomancak, and Albert Cardona. Fiji: an open-source platform for biological-image analysis. 9(7):676–682. Number: 7 Publisher: Nature Publishing Group.
- [61] Emerson Gehr, Abbie Terrell, Katrina Vermillion, and Alexandria Mendoza. Structural states of filamentary microgravity dusty plasma. *Physics of Plasma*, 2024.
- [62] Till Daniel Frank. *Nonlinear Fokker-Planck equations: fundamentals and applications*. Springer series in synergetics. Springer. OCLC: ocm57476591.
- [63] Constantino Tsallis. *Introduction to Nonextensive Statistical Mechanics: Approaching a Complex World*. Springer, New York, 2009th edition edition, 2009.
- [64] J L Padgett, E G Kostadinova, C D Liaw, K Busse, L S Matthews, and T W Hyde. Anomalous diffusion in one-dimensional disordered systems: a discrete fractional Laplacian method. *Journal of Physics A: Mathematical and Theoretical*, April 2020.
- [65] Nahla Ben Salah. Some properties of q-gaussian distributions, 2021.
- [66] Zahra Ghannad. Identification of time scales of the violation of the stokes–einstein relation in yukawa liquids. *Physics of Plasmas*, 28(4), April 2021.
- [67] Constantino Tsallis. Possible generalization of boltzmann-gibbs statistics. 52(1):479–487.
- [68] A. Shivanandan, A. Radenovic, and I. F. Sbalzarini. Mosaicia: an imagej/fiji plugin for spatial pattern and interaction analysis. *BMC Bioinformatics*, 14:349, 2013.
- [69] K. Avinash, R.L. Merlino, and P.K. Shukla. Anomalous dust temperature in dusty plasma experiments. *Physics Letters A*, 375(30–31):2854–2857, July 2011.
- [70] Jiulin Du. Nonextensivity in nonequilibrium plasma systems with Coulombian long-range interactions. *Physics Letters A*, 2004.
- [71] Yu Haining and Du Jiulin. The nonextensive parameter for nonequilibrium plasmas in magnetic field. 350:302–309.
- [72] R. A. Treumann, C. H. Jaroschek, and M. Scholer. Stationary plasma states far from equilibrium. *Physics of Plasmas*, April 2004.
- [73] G. Livadiotis, M. I. Desai, and L. B. Wilson. Generation of Kappa Distributions in Solar Wind at 1 au. *The Astrophysical Journal*, 2018.
- [74] M. P. Leubner and Z. Voros. A nonextensive entropy approach to solar wind intermittency. 618(1):547–555.
- [75] Constantino Tsallis, Joao C Anjos, and Ernesto P Borges. Fluxes of cosmic rays: a delicately balanced stationary state. *Physics Letters A*, 2003.

- [76] L. F. Burlaga and A. F.-Viñas. Tsallis distributions of the large-scale magnetic field strength fluctuations in the solar wind from 7 to 87 au. *Journal of Geophysical Research: Space Physics*, 110(A7), July 2005.